Quartz-enhanced photoacoustic spectroscopy for gas sensing applications

15

Vincenzo Spagnolo[a], *Pietro Patimisco*[a], *Frank K. Tittel*[b]
[a]Technical University of Bari, Bari, Italy, [b]Rice University, Houston, TX, United States

15.1 Introduction

The detection and measurement of trace gas concentrations is important for a wide variety of applications, including environmental monitoring, industrial process control analysis, biomedicine, combustion processes, and the detection of toxic and hazardous gases. For example, trace gas sensors with high detection sensitivity and selectivity are required in atmospheric science for the monitoring of different trace gas species, including greenhouse gases and ozone, while in breath diagnostics, gas species such as nitric oxide, ethane, ammonia, and numerous others are used as biomarkers. Techniques based on laser absorption spectroscopy (LAS) for trace gas sensing, compared to other techniques, are considerably faster with response times <1 s, exhibit minimal drift, offer high gas specificity, are capable of part-per-quadrillion (ppq) detection sensitivity, and permit real-time in situ measurements [1, 2]. The principle of molecular absorption is based on the transitions that an electromagnetic wave causes in a chemical species. If a molecule is irradiated by infrared light, it is excited to a rotational-vibrational energy level manifold. Absorption lines are specific for each chemical species. LAS-based techniques offer not only excellent detection sensitivity and selectivity but also long effective optical path lengths, compactness, mechanical stability, versatility, and cost-effectiveness. In the case of cavity ring-down spectroscopy (CRDS), an optical cavity with two concave mirrors with low loss and high reflectivity (>99.9%) provides a long optical path of up to several kilometers. A light pulse is injected into the cavity through one of the mirrors, and inside the cavity multiple reflections occur. After each reflection, leakage radiation from the cavity is registered by means of an appropriate photodetector [3]. A modification of the CRDS is cavity-enhanced absorption spectroscopy (CEAS) in which the radiation is injected at a very small angle respect to the cavity axes, which results in the formation of a dense structure of weak optical axial modes that makes the entire system more robust against instability in both the cavity and laser spectrum [4]. The idea of integrated cavity output spectroscopy (ICOS) is similar to CEAS. However, the measurement procedure is based on the comparison between signal amplitude at both the input and the output of the cavity [5]. Both techniques require precise information about mirror reflectivity, a sensitive photodetector with a fast response, perfect optical alignment, and the use of long optical path lengths.

Mid-infrared Optoelectronics. https://doi.org/10.1016/B978-0-08-102709-7.00015-2

One of the most robust and sensitive trace gas optical detection techniques is photoacoustic spectroscopy (PAS), which has extremely high detection sensitivities with a compact and relatively low-cost absorption detection module [6]. PAS is based on an optical absorption process, such as other optical detection techniques, but differs in the physical phenomenon used for the detection of the absorption signal. When light at a specific wavelength is absorbed by the gas sample, the excited molecules will subsequently relax to the ground state either through emission of photons or by means of nonradiative processes. These processes produce localized heating in the gas, which in turn results in an increase in the local pressure. If the incident light intensity is modulated, the generation of thermal energy in the sample will also be periodic, and a pressure wave, i.e., a sound wave, will be produced having the same frequency of light modulation. The key advantage of this technique is that no optical detector is required and the resulting sound waves can be detected with a commercial hearing aid or a microphone. PAS is a widely used method for trace gas detection. PAS was used by Viengerov [7] for the first spectroscopic gas analysis in 1938 to study infrared light absorption in gas mixtures. Subsequently, Luft [8] obtained a minimum detection limit (MDL) of a PAS system down to part-per-million (ppm) concentration, even with radiation sources of low spectral brightness. Kerr and Atwood [9] used for the first time a continuous-wave (CW) CO_2 laser as a radiation source to detect CO_2 in nitrogen. Kreuzer [10] reported the detection of methane with an MDL of 10 parts per billion (ppb) using a HeNe laser as the light source. Trace gas detection with a PAS system was studied by Max and Rosengren using a resonant PA gas cell, showing that the MDL of gas detection is determined by microphone and preamplifier noise [11]. They showed that the acoustic noise detected with the microphone is mainly determined by a reachable MDL. They employed a CO_2 laser as the light source for trace amounts of NH_3 in gas detection. With a laser power of 280 mW, they reached an MDL of 3 ppb. Busse and Bullemer obtained a PAS spectrum of methanol vapor using a commercial Fourier transform infrared spectrometer and a microphone in an absorption cell, providing a comparison of a conventional mid-infrared absorption spectrum with a PAS spectrum, with the same experimental conditions [12]. PAS is capable of performing trace gas measurements at sub-part-per-trillion (ppt) concentration levels, by combining PAS systems with different approaches. For example, T. Tomberg combined a highly sensitive cantilever-enhanced photoacoustic detector; a stable high-power, narrow-linewidth, mid-infrared CW optical parametric oscillator; and a strong absorption cross section of hydrogen fluoride to demonstrate the ability of cantilever-enhanced photoacoustic spectroscopy to reach a sub-ppt (650 ppq)-level sensitivity in trace gas detection [2]. Other advantages of PAS include a small size, a large linear dynamic range (from a small percentage to ppt concentration) and a long-term stability [6]. These advantages make the PAS technology competitive with, and in many cases preferred to, other trace gas-sensing methods. The PAS signal can be amplified by tuning the modulation frequency to one of the acoustic resonances of the gas sample cell. The photoacoustic signal S can be expressed as:

$$S = CP_L\alpha \tag{15.1}$$

where C is the instrumental constant, P_L is the laser power, and α is the gas absorption coefficient that is equal to $\alpha = N_{tot}\sigma c$, where σ is the cross section of the optical transition, c is the concentration of the target gas, and N_{tot} is the total number of molecules per unit volume. From Eq. (15.1), it follows that the PAS signal is proportional to the sample concentration. The minimum optical absorption coefficient α_{min} detectable with a PAS-based sensor is determined by the condition $S=N$, where N is the noise level, which is assumed to be independent from optical excitation. Hence, the minimum detectable concentration c_{min} can be expressed using Eq. (15.2) as:

$$c_{\min} = \frac{\alpha_{\min}}{N\sigma} \tag{15.2}$$

The instrumental constant C in Eq. (15.1) depends on the cell size and geometry, modulation frequency of the radiation, efficiency of the transducer, and quality factor Q of the acoustic resonance defined by:

$$Q = \frac{f_0}{\Delta f_{FWHM}} \tag{15.3}$$

where f_0 and Δf_{FWHM} are the resonant frequency and the full width at half maximum (FWHM) of the resonance profile, respectively. The quality factor Q and f_0 can be experimentally measured and typically fall in the ranges 40–200 and 1000–4000 Hz, respectively. The effective resonator integration time is usually defined as $\tau_r = Q/f_0$. One of the highest reported values is τ_r=56 ms [6]. Achieving longer integration times in a gas-filled resonator is problematic because of intrinsic losses related to gas viscosity and other relaxation processes. The development of high-power laser sources, sensitive microphones, lock-in detection and amplification schemes, and optimized resonant acoustic cells provided a big boost to improve the PAS systems. CW single-mode diode lasers, optical parameter oscillators in the near-IR, and interband quantum cascade lasers (ICLs) and quantum cascade lasers (QCLs) in the mid-IR have been successfully applied in PAS [6]. Compact photoacoustic gas sensors based on broadband IR sources have been also reported [13]. Resonant PAS cells and optical fiber amplifiers have been developed to enhance PAS detection sensitivity [14]. The MDL has been improved by studying and analyzing the main noise contributions affecting a PAS system. The three main noise sources are (i) noise caused by the radiation that is incident upon the walls of the PAS absorption cell, (ii) nonselective absorption of the gas cell window, and (iii) external acoustic noise. In order to improve the signal-to-noise ratio (SNR), different designs for PAS cells have been proposed and implemented, including a resonant cell with acoustic buffers, windowless and a differential cell [15]. A schematic of a PAS setup employing a differential acoustic cell is depicted in Fig. 15.1.

A differential cell includes two acoustic resonators equipped with microphones having the same responsivity at the resonance frequency of the PAS cell. Since the laser light excites only one of the two resonators, the difference between the two signals removes noise components that are coherent in both resonators.

PAS has been successfully applied to trace gas-sensing applications, which include atmospheric chemistry, volcanic activity, agriculture, industrial processes, workplace

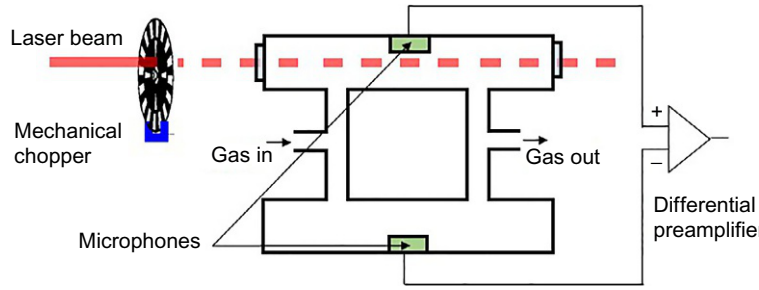

Fig. 15.1 PAS system with a differential acoustic cell composed of two acoustic resonators. A microphone is located in the center of each cell. Although only one resonator is illuminated by a laser ray, acoustic waves at the cell resonance frequency are generated in both cells. The PAS signals from microphones are subtracted by a differential amplifier.

surveillance, and medical diagnostics. For instance, PAS has been used to monitor NO from vehicle exhaust emissions, which contributes to respiratory allergic diseases, inflammatory lung diseases, bronchial asthma, and the depletion of ozone [16]. Other applications include monitoring respiratory NH_3 emission from cockroaches as well as detecting the intake of prohibited substances by athletes [17]. Low-cost portable PAS sensors have been available on the market, examples of which include smoke detectors, toxic gas monitors, and oil sensors for monitoring hydrocarbons in water.

15.2 Fundamentals of QEPAS

The research team of Kosterev and Tittel at Rice University reported in 2002 the first demonstration of a novel technique based on PAS and named quartz-enhanced PAS (QEPAS) [18]. In less than a decade, QEPAS has been used to obtain spectra of many gas species. Mid-, near-, and far-infrared lasers, as well as optical parametric oscillators have been employed as radiation sources in QEPAS systems described in numerous publications [19]. The basic idea of QEPAS is to accumulate the acoustic energy in a sharply resonant acoustic transducer, avoiding the use of acoustic gas cells, thereby removing restrictions imposed on the gas cell design by the acoustic resonance conditions. A quartz tuning fork (QTF) is positioned in the acoustic near-field zone of the focused laser beam and the cell only serves to separate the target sample from the surrounding environment and fix and control its pressure. QTFs are perfect candidates to detect weak photoacoustic excitation since they are characterized by a sharp resonant acoustic profile. The sound wave generated between the two prongs causes an antisymmetric vibration of the prong in the QTF plane. In Fig. 15.2A the first in-plane flexural antisymmetric mode caused by a sound wave located between the two QTF prongs is schematically represented. This vibration mode is piezoelectrically active and thus electrical charges are generated, proportional to the sound wave intensity. QTFs operating in the few kilohertz range can be used since the energy transfer processes in gases occur on a microsecond time scale [20] and the PAS signal decreases

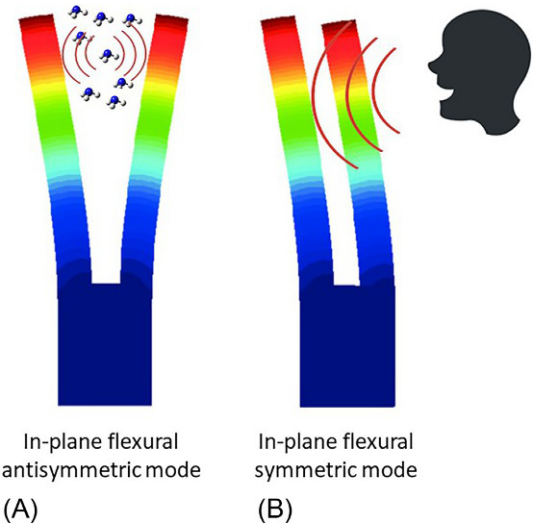

Fig. 15.2 First in-plane flexural antisymmetric (A) and symmetric (B) mode of a QTF. The contour of the displacement field is shown in color.

at higher frequencies. The most convenient QTF used in electronic timing devices, such as clocks and smartphones as frequency standards, has a resonance frequency of 32768 (2^{15}) Hz in vacuum. A 32.7-kHz QTF was the only QTF employed in QEPAS sensor systems for the first 10 years after the invention of this technique in 2002 [18].

The most important advantages of QEPAS include the following features: (i) a high resonance frequency of the tuning fork (~32.8 kHz) combined with narrow bandwidth (a few hertz at atmospheric pressure) that yields a very high Q>10,000; (ii) applicability over a wide range of pressure, including atmospheric pressure; (iii) the capability to analyze trace gas samples as low as few cm^3 in volume; and (iv) a QTF is not spectrally sensitive and is practically unaffected by environmental noise. Insensitivity to environmental noise in QEPAS derives from two physical phenomena. First, a QTF is an acoustic quadrupole resonator with a Δf_{FWHM} of a few hertz at normal pressure, so only an insignificant number of frequency components in this narrow spectral band can produce efficient excitation of the QTF vibrations. Sound waves in air at 32 kHz have an acoustic wavelength ~1 cm and, thus, if produced by external acoustic sources, such waves tend to apply a force in the same direction on the two QTF prongs (in-plane symmetric mode, as depicted in Fig. 15.2B) positioned at a distance lower than 1 mm. The resulting deflection of QTF prongs is not piezoelectrically active and in contrast with the antisymmetric vibration does not yield a detectable signal. Second, ambient noise is generally low above 10 kHz and, therefore, has a minimal effect on the QEPAS signal. In other words, insignificant environmental noise falls within the analyzed bandwidth. The only way to cause QTF to vibrate via the photoacoustic effect is to produce sound waves from an acoustic source located between the two QTF prongs. The standard way to realize such a condition is to focus the excitation laser beam through the gap between the prongs on the QTF crystal plane.

Similar to PAS-based sensing systems, the detection sensitivities of QEPAS sensor systems are proportional to the exciting laser optical power [18, 19, 21]. The generation of a photoacoustic wave involves the energy transfer from internal to translational molecular degrees of freedom. If a rotational-vibrational state is excited, a collision-induced vibrational to translation (V-T) relaxation follows, with a time constant that for a particular molecule is dependent on the presence of other molecules and intermolecular interactions. When QEPAS measurements are performed at a detection frequency of ~32.7 kHz, the system will be more sensitive to the V-T relaxation rate compared to the conventional PAS, which is commonly performed at f_0<4 kHz. In case of a slow V-T relaxation with respect to the modulation frequency, the thermal waves in the gas cannot follow fast changes of the laser-induced molecular vibration excitation. Thus, the generated photoacoustic wave is weaker than it would be in case of a fast V-T energy equilibration [22]. The photoacoustic signal S is related to the relaxation time as follows [23]:

$$S = \frac{Q \cdot P_L \cdot \alpha}{\sqrt{1 + \left(2\pi f_0 \tau_{V-T}\right)^2}} \tag{15.4}$$

where $\tau_{V\text{-}T}$ is the V-T relaxation time. S_0=$QP_L\alpha$ is the photoacoustic signal as it would be for an instantaneous relaxation ($\tau_{V\text{-}T}$=0). To enhance the energy relaxation rate, relaxation promoters (typically H_2O or SF_6) are added to the gas sample mixture [19]. Using this approach, enhancements of two orders of magnitude in the QEPAS signal have been reported [24, 25]. This requires accurate measurements of the promoter concentration and additional sensor calibration.

15.2.1 Quartz tuning fork

The QTF represents the core of any QEPAS sensor. A tuning fork can be considered to be composed by two cantilevers bars (prongs) joined at a common base. As discussed in Section 15.2, the in-plane flexural modes of vibrations of the QTFs can be classified into two groups: symmetrical modes, in which case the prongs move along the same direction and antisymmetrical modes, in which case the two prongs oscillate along opposite directions (see Fig. 15.2). The in-plane antisymmetrical modes will be the predominant modes when a sound source is positioned between the prongs, forcing them to move in the opposite directions. In QEPAS sensors, the light source (typically a laser) is focused between the QTF prongs and sound waves produced by the modulated absorption force prongs to vibrate antisymmetrically back and forth. QTFs can be designed to resonate at any frequency in the 3–200 kHz range and beyond, since resonance frequencies are defined by the properties of the piezoelectric material and by its geometry [26]. The interaction between the laser modulated beam and a trace gas leads to the generation of acoustic waves that mechanically bend the QTF prongs. Hence, the electrode pairs of the QTF will be electrically charged due to the quartz piezoelectricity. Piezoelectricity is the coupling between internal dielectric polarization and strain, and is present in most crystals lacking a center of inversion symmetry. When a stress is applied to these materials, it induces a displacement of charge and a net electric field. The effect is reversible: when a voltage in applied across a

piezoelectric material, it is accompanied by a strain. Due to this intrinsic coupling of strain and charge displacement, a QTF can be modeled both electrically and mechanically, each prong being modeled as a slab as shown in Fig. 15.3A–C.

Both mechanical motion and electrical response can be modeled using differential equations, having equivalent mathematical forms. Thus, a QTF can be represented by a circuit with a capacitance C, a resistance R and an inductance L_i and an equivalent mass m on a spring, with spring constant k and damping factor β. The electrical model of the tuning fork differs from the classical damped oscillator by the presence of a capacitor C_p parallel to the RLC series components. The two domains can be coupled through a relation, in which the force driving the QTF is proportional to the driving voltage. Hence, a voltage signal measured from the QTF can easily translate into the force on it. The most commonly used approach is to acquire the QTF electrical response using an ultralow transimpedance amplifier with a feedback resistor. Feedback maintains a zero voltage between the QTF electrodes and so that the influence of a parallel stray capacitance is minimized. In this condition, the QTF model is reduced to an RLC series circuit and the resonant frequency is given by:

$$f_0 = \frac{1}{2\pi}\sqrt{\frac{1}{L_i C}} \tag{15.5}$$

and the Q-factor is:

$$Q = \frac{1}{R}\sqrt{\frac{L_i}{C}} \tag{15.6}$$

while the impedance of the RLC circuit at the resonance condition is equal to its resistance.

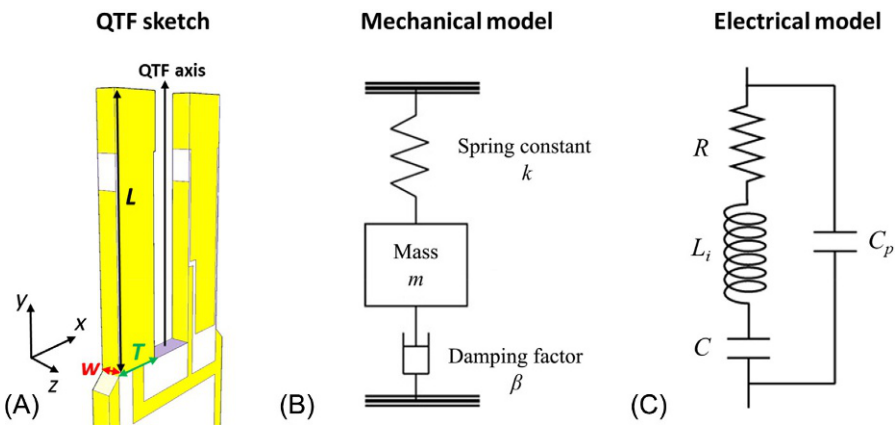

Fig. 15.3 (A) Schematic view of QTF dimensions. L and T are the prong length and thickness, respectively, and w is the crystal thickness. The QTF axis is located between the two prongs, parallel to the y-axis. (B) Mechanical models of a QTF. (C) Electrical model of a QTF. R, L, and C are the electrical resistance, inductance, and capacitance of the QTF, respectively. C_p is its parasitic capacitance.

The QEPAS sensor noise measured at the amplifier output at the resonant frequency is ultimately determined by the thermal noise of the equivalent resistor R [27]:

$$\frac{\sqrt{(V_N{}^2)}}{\sqrt{\Delta f}} = R_f \sqrt{\frac{4KT_e}{R}} \tag{15.7}$$

where V_N is the voltage noise at the transimpedance amplifier output, Δf is the detection bandwidth and T_e is the QTF temperature. The feedback resistor also introduces noise, which is several times lower than the thermal QTF noise and can be neglected for typical values of R in the range 10–100 KΩ. Due to the piezoelectricity of quartz, when a stress is applied to a QTF prong, a displacement of charge and a net electric field is induced. The effect is reversible and when a voltage is applied to a piezoelectric material, it is accompanied by strain. Hence, the QTF resonance parameters, i.e., the resonance frequency, the quality factor, and the electrical resistance can be measured by exciting the resonator electrically. A sinusoidal voltage excitation results in a piezoelectric charge distribution across the QTF prongs. This piezoelectric current is ~~then~~ converted to an output voltage by means of the transimpedance amplifier and then demodulated by a lock-in amplifier [26, 28]. The maximum of the $I_{QTF}(f)$ function, where I_{QTF} is the QTF current and f is the modulation frequency of the applied voltage, yields the resonant frequency f_0. The Lorentzian fit of $I_{QTF}(f)$ provides Δf_{FWHM}. In this way, R and Q are determined by using the relation $R=V/I_{QTF}(f_0)$ and Eq. (15.3). The other two electrical parameters, L_i and C, can be then estimated by using Eqs. (15.5) and (15.6).

15.2.2 Dual-tube acoustic microresonators (on-beam)

Significant enhancements of the QEPAS SNR have also been obtained as a result of the implementation of microresonators (mRs). A mR is composed by one or two thin tubes and the QTF is positioned either between (on-beam [OB] QEPAS) [29] or adjacent to the tube(s) (off-beam QEPAS) [30, 31] to probe the acoustic vibration excited in the gas contained inside the tubes. A system composed of the QTF and the mR is called a spectrophone or acoustic detection module (ADM). In all QEPAS sensor configurations, it is critical to avoid that photoacoustic exciting radiation hits the ADM, otherwise an undesirable background that can be several times larger than the QTF thermal noise level arises, with a shifting fringe-like interference pattern shape, which limits the detection sensitivity [32]. The effect of tubes is to amplify the sound wave generated within the absorbing gas. As discussed in previous sections, a QTF is a high-Q resonator with a narrow passband. A resonator tube is low-Q acoustic element. When the air-filled mR tube and the QTF are acoustically coupled to form a spectrophone, resonance properties are affected: the resonance frequency is slightly shifted, and the quality factor is reduced, suggesting that QTF loses energy via interaction with the low-Q acoustic tube [29]. A qualitative representation of the impact of tubes on the resonance frequency and quality factor of a bare QTF is given in Fig. 15.4.

The influence of the spectrophone design parameters on QEPAS performance when a 32.7-kHz QTF is employed has been investigated in Refs. [19, 29]. The first parameter to be optimized is the position of both tubes along the QTF axis.

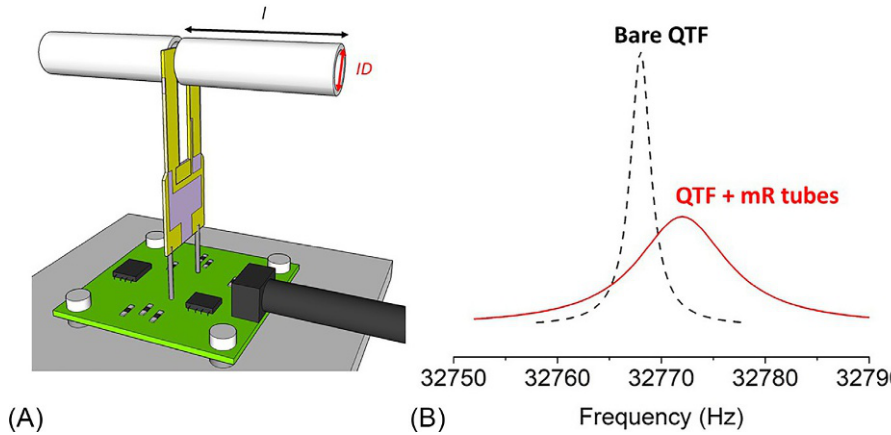

Fig. 15.4 (A) Sketch of an ADM composed by a QTF and a pair of mR tubes. (B) Resonance curve of a bare QTF (*black dashed line*) and of a QTF when acoustically coupled with a pair of resonator tubes (*solid red line*). The impact of the resonator tubes is to shift the resonance frequency and increase the FWHM value.

The acoustic source can be supposed to be located between the prongs. A simplified model is described in Ref. [19] which considers the total momentum of a pressure force acting on the two prongs of the QTF. The main assumptions are (i) two prongs, which radiate as point sources and create divergent spherical-shaped sound waves (monopole approximation); (ii) the intensity of the pressure wave decreases as the inverse of the distance and is assumed to be constant along the thickness of each prong; and (iii) the acoustic coupling between two oscillating prongs can be neglected (small oscillations approximation). The theoretical model predicts the experimentally observed optimal vertical position of the laser beam, occurring on the QTF axis (see Fig. 15.3A), ~0.3 mm far from the QTF top. A more detailed and detailed theoretical model for the determination of the beam position of the laser beam that maximizes the QEPAS signal was proposed in Ref. [33]. The model consists of three stages. First, an explicit formula was derived for the acoustic pressure wave by using the cylindrical symmetry of the laser beam and a narrow width of the tuning fork resonance to reduce the inhomogeneous wave equation to a Bessel equation. The model shows that the amplitude of the pressure wave is proportional to the laser modulation frequency. Then, the Euler-Bernoulli equation was employed to model the resonant vibration of the prongs of the QTF. Finally, the well-known electromechanical relationships for QTFs was used to calculate the piezoelectric current generated by the mechanical vibration. In spite of these simplifying assumptions, an excellent agreement between theory and experiments was found and the optimal vertical position of the focused laser beam occurs on QTF axis, at y~0.3 mm, equal to the result of simplified mechanical model.

When QTF is coupled with a pair of mR tubes, the geometrical parameters influencing the sensor performance are the internal diameter ID and the length l of the two tubes together with the spacing between the tube and the surface of the QTF. The length of two tubes is correlated with the sound wavelength, given by $\lambda_s = v_s/f$, where v

is the speed of the sound (343 m/s in air). For f=32,786, λ_s is 10.5 mm. Assuming that the left and right tubes can be considered as a single tube neglecting the gap, each tube should be cut to a $\lambda_s/4$ length (l=2.63 mm) to form a half-wave resonator. Instead, if the gap between the tubes is big enough to make them almost independent, the tube length should be $\lambda_s/2$ (l=5.25 mm). Experimental studies showed that l=4.4 mm (internal diameter of 0.6 mm and external one of 0.9 mm) yields the highest SNR (~2700), which is ~30 times higher than that of a bare 32.7 kHz QTF at atmospheric pressure [29]. Thus, the optimal tube length falls between $\lambda_s/4$ and $\lambda_s/2$, because of the interaction of two resonator tubes and their acoustic coupling with the QTF. This observation is supported by a decrease of the Q-factor from ~14,000 (bare QTF) to 3400. The Q-factor provides also a measure of the acoustic coupling between the QTF and tubes, since a high-Q QTF loses energy primarily via coupling to the low-Q tubes [34]. The QEPAS SNR is dependent on the tube length l and variations as small as 0.6 mm reduce this ratio to ~1900. The choice of the optimal ID can be related to the QTF prong spacing. When the tube diameter is larger than the prong spacing, the gap between two tubes becomes less important and the tubes are acoustically coupled with the QTF. With an internal diameter of 0.84 mm (~3 times the prong spacing) the optical length is 3.9 mm (SNR~2400), closer to a $\lambda_s/4$ length with respect to the case with l=4.4 mm, confirming the above assumption. Consequently, a large decrease of the Q-factor was also observed (from ~3400 to ~1700). When the tube diameter becomes comparable with the prong spacing, the acoustic coupling is reduced and the SNR decreases. For an ID=0.41 mm, the Q-factor increased up to ~7500 and the SNR was reduced to ~2400 [29]. The gap size between the QTF and the tubes is a difficult parameter to be controlled during the spectrophone assembly and has a significant effect on the final QTF performance. With a large gap, the diverging flow from the two tubes ends cannot efficiently push against the QTF prong. Therefore, the gap should not be wider than 50 µm; when the gap is reduced from 50 to 25 µm and the SNR increases by 13% [29].

15.2.3 Wavelength modulation and dual-frequency detection

The combination of single-mode emission and fast tunability makes semiconductor lasers extremely attractive for sensitive trace gas detection. When these features are combined with modulation techniques, high detection sensitivities can be achieved [35, 36]. In wavelength modulation (WM), the frequency of the laser light is modulated with a periodic function, typically a sine wave. One important advantage of WM is that only the noise centered at the detection frequency and within the detection bandwidth will affect trace gas measurements. The interaction between the chemical species to be detected and the modulated light leads to the generation of signals at the modulation frequency and its harmonics. Each harmonic of the analytical WM signal can be detected coherently with phase-sensitive detection electronics based on a lock-in amplifier. For gas-sensing techniques based on cavity-enhanced and multipass absorption cell, the choice of modulation frequency is often limited by the detector bandwidth. The detection band should be high enough in order to limit $1/f$ laser noise. However, exceeding 100 kHz is not convenient because the noise levels off [37]. In QEPAS, the modulation frequency should match the resonance frequency

of the QTF or its sub-harmonics. When the laser injection current $i(t)$ is modulated at an angular frequency $\omega=2\pi f$, $i(t)=i_0+\Delta i\cdot\cos\omega t$, the light intensity (or optical power) $I(t)=I_0+\Delta I\cdot\cos\omega t$ and the instantaneous laser frequency $\nu(t)=\nu_0+\Delta\nu\cdot\cos(\omega t+\psi)$ are simultaneously modulated, as schematically depicted in Fig. 15.5A. The lock-in amplifier output records the variation of the amplitude (the envelope) of a selected harmonic of the modulation frequency. Higher harmonics are generated due to the nonlinearity in the absorption coefficient $\alpha[\nu(t)]$ at the center frequencyν_0. For $\Delta\nu\ll$FWHM of the absorption profile, all harmonics can be extracted from a Taylor-series expansion of the absorption line shape $\alpha[\nu(t)]$ at ν_0 and the expression for the 1f signal I_{1f} at a frequency $f=\omega/2\pi$ becomes [19, 38–40]:

$$I_{1f} = \Delta I\cos(\omega t) - \Delta I\alpha(\upsilon_0)L_p\cos(\omega t) - I_0\alpha'(\upsilon_0)\Delta\upsilon\cos(\omega t+\psi)L_p \tag{15.8}$$

where L_p is the length of the optical path. The first term is the background signal, which is independent of the gas concentration and intensity I_0, but depends on how ΔI varies with Δi. The second term is an absorption-dependent contribution and the third term is the first derivative signal arising from WM. The phase of the first derivative contribution is shifted by ψ from the second term. Thus, even for a small amplitude and frequency modulation, the 1f signal profile is not a true first derivative of the line-shape, but is distorted by the presence of the second term. The I_{1f} trend as a function of the laser frequency across a Lorentzian absorption line is reported in Fig. 15.5B. The 2f signal I_{2f} has the form:

$$\begin{aligned} I_{2f} &= -\Delta I\alpha'(\upsilon_0)\Delta\upsilon\cos(\omega t)\cos(\omega t+\psi)L_p \\ &\quad + \frac{1}{4}I_0\alpha''(\upsilon_0)\Delta\upsilon^2\cos\left[2(\omega t+\psi)\right]L_p \end{aligned} \tag{15.9}$$

In this case, the first term is due to the residual amplitude modulation (RAM) and is proportional to the first derivative of the absorption, whereas the second term represents the second-derivative term, arising from WM (with a phase difference of ψ between the terms). Hence, the 2f signal profile is not a true second derivative of the absorption line shape, even for a small $\Delta\nu$, but is distorted by a contribution originating from the RAM that unbalances the two minima (see Fig. 15.5C). Hence, the detection at twice the applied modulation frequency (2f detection) is preferred. The acquired signal will show a background-free second harmonic derivative line-shape and the effect of RAM appears only as a distortion of the line-shape.

When WM technique is combined with QEPAS, the laser light is modulated at a half of the QTF resonance frequency, $f_0/2$ and QEPAS signal is demodulated at f_0. In this case, the QTF detects sound oscillations at the second harmonic of the modulation frequency caused by the double intersection of the absorption line by the laser line during a modulation period.

15.2.4 Amplitude modulation and broadband absorbers

When operating in WM, a strong background signal was observed for the 1f detection, originating from stray light ending up on the walls of the ADM [19]. This is confirmed by the observation that the amplitude of this offset strongly increases with

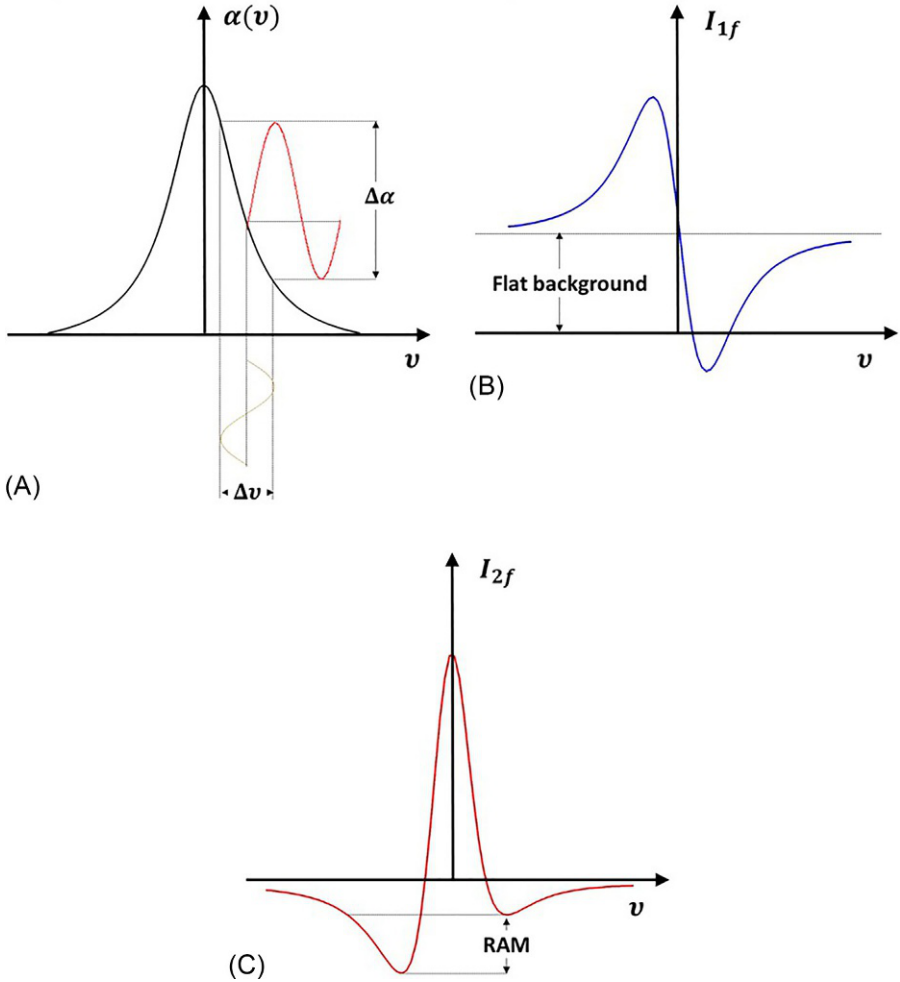

Fig. 15.5 (A) WM based on a Lorentzian absorption line shape. (B) Absorption profile in WM and 1*f* detection: the profile resembles the first derivative of a Lorentzian absorption line shape with a flat background. (C) Absorption profile in WM and 2*f* detection: the 2*f* signal profile is not a true second derivative of a Lorentzian absorption line shape, but it is distorted by a contribution originating from the RAM which unbalances the two minima.

a misalignment of the laser beam in lateral directions so that the beam wings touch the QTF. Instead, it was experimentally observed that the 2*f* detection is background-free. Distortions in the demodulated signal displaying an asymmetry on both side of the spectrum around the peak can be associated to an amplitude intrinsic modulation contribution, which is introduced by current modulation. Vibrational spectra of most molecules consisting of more than five atoms are so dense that infrared absorption spectra of such polyatomic molecules consist of 100–200 cm^{-1} broad bands. Spectroscopic identification of these species requires laser excitation sources with a wide spectral

coverage. However, distributed feedback (DFB) or Fabry-Perot (FP) QCLs cannot be wavelength modulated with a sufficient spectral tuning coverage for broadband absorption features. Thus, QEPAS detection of such molecules will require amplitude modulation (AM) of the laser radiation. The laser intensity is modulated at f_0 by means of square wave amplitude current modulation and the QEPAS signal is detected by a lock-in amplifier at the same f_0 frequency. Unlike WM QEPAS, AM QEPAS is not background-free. Residual absorption of laser radiation by the cell windows as well as scattered radiation absorbed inside the gas cell produce a sound at the QTF resonance frequency, thus generating a coherent background. However, this background can be stable over several hours, which allows background subtraction. Typically, for every spectral point, both signal and background components normalized to the laser power are acquired. In post-processing, the in-phase and the quadrature components of the demodulated photoacoustic signal were acquired and by vector subtraction it is possible to remove the background signal [27, 41, 42].

15.3 QEPAS configurations

Acoustic mR tubes are important components that are acoustically coupled with QTFs to improve the performance of QEPAS sensors. Even if OB alignment (two thin tubes aligned perpendicular to the QTF plane, or one single tube with two slits is located through the prong gap) represented the most convenient configuration in terms of signal-to-noise enhancement for a QEPAS sensor, several configurations have been proposed in last few years. Indeed, the OB-QEPAS configuration suffers minimal disadvantages, such as (i) the resonant acoustic wave condition was not exactly obtained; (ii) the open-ended tubes introduce sound energy-losses; and (iii) the gap between the 32.7 KHz QTF prongs is only ~300 µm wide, which limits the inner diameter of the mR and thus the size of the laser beam that passes through the tubes. In this paragraph, different spectrophone configurations proposed so far will be reviewed, pointing out merits and disadvantages with respect to the OB configuration.

15.3.1 Off-beam

Off-beam QEPAS was first reported in Ref. [30]. In off-beam QEPAS, a single mR is placed alongside the QTF which senses the pressure in the mR through a small aperture. A sketch of the off-beam QEPAS configuration is reported in Fig. 15.6A.

Thus, the mR tube length is determined by the first longitudinal mode of the acoustic wave at f_0. For this mode, the resonant acoustic pressure antinode is located at the center of the mR. Hence, a small slit is cut in the middle of the mR and the QTF is coupled to the mR by placing it laterally to the mR tube close to the centrally located slit. The off-beam QEPAS configuration results in certain technical advantages as it facilitates the optical alignment and allows more flexibility in the selection of QTF dimensions. As in the OB configuration, the acoustic oscillations of the gas are excited in the mR by the intensity modulation induced by the laser source. The photoacoustic

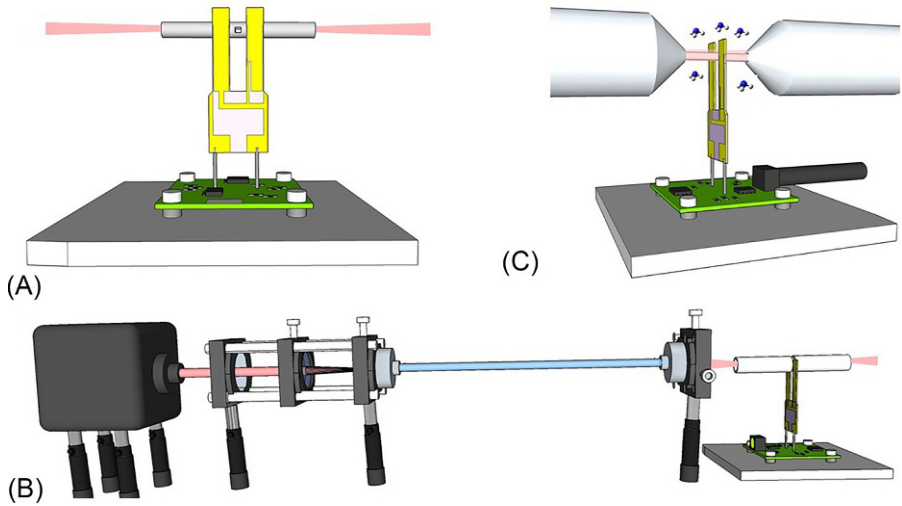

Fig. 15.6 (A) Schematic of an off-beam QEPAS configuration. A single tube with a small slit is placed alongside the QTF. (B) Fiber-coupled QEPAS sensor. A lens is used to focus a collimated laser beam into the hollow core waveguide entrance, and a focusing optics placed at the waveguide exit allows the focalization of the laser beam through the two mR tubes without hitting them. (C) Schematic of the evanescent-wave QEPAS. A tapered fiber is threaded through the gap between the two prongs of the QTF.

signal amplitude S in the mR can be expressed as $S=C_G(f)\alpha P_L$ where $C_G(f)$ is a geometrical parameter that describes the characteristics of the mR at a given frequency f. The acoustic oscillations in the mR give rise to sound waves radiated via a slit at its center and are detected by the QTF placed outside the mR close to the slit. To maximize sound energy coupling, the distance between the mR and the QTF must be carefully chosen, since a long distance will decrease the acoustic coupling between mR and QTF, while too a short distance will dampen the QTF vibration, because of viscous drag effects. Liu et al. [30] have shown that the close proximity of the QTF to mR results in optimum acoustic coupling. At the same time, viscous drag in the air layer between the QTF and mR reduces the Q-factor. Consequentially, the SNR increases by enlarging the gap up to a value of 5 µm and then decreases for wider QTF gaps. At atmospheric pressure, Q-factors from 13,000 to 8000 are achieved indicating relatively weak mR coupling to the QTF compared to the OB configuration, where the Q changes from 13,000 to as low as 1380. A maximum off-beam QEPAS signal was obtained when the mR slit was positioned between 1 and 1.5 mm below the QTF opening, as observed in the case of the OB-QEPAS configuration. Liu et al. [31] performed an experimental investigation of the dependence of the off-beam QEPAS signal as a function of the mR length and inner diameter. They observed that the inner diameter-to-optical length ratio linearly increases with the inner diameter. Once the inner diameter is chosen for a specific application, the optimal ratio can be determined. In addition, for efficient coupling of the acoustic signal from the mR to the QTF via a

slit, it is also necessary to optimize the slit size. A small slit size limits the coupling of the acoustic energy, while a large slit size disperses the output sound energy. Varying the tube length, the resonant frequency of the mR shifts and the QTF operates as a fixed-frequency probe. By using the theory of finger-holes in woodwind instruments it is possible to find a relation between the tube length and the mR resonance. According to this theory, the tube length corresponding to f_0=32,750 Hz is l=7.56 mm. Liu et al. found experimentally an optimal slit width of ~0.15 mm with a length of ~0.4 mm, for a mR with an outer diameter of 0.7 mm, an inner diameter of 0.45 mm and a length of 8 mm [31]. For these optimal conditions, a photoacoustic signal of ~15.7 times higher than that corresponding to a QEPAS system using a bare QTF is obtained. Compared to the OB design, the SNR is reduced by a factor of ~1.7 at atmospheric pressure. However, off-beam QEPAS is more flexible in terms of the QTF geometry employing custom-made QTFs, with a smaller gap between the prongs without complications related to using an optimized excitation laser pump beam. An off-beam QEPAS spectrophone is also technologically easier to assemble and align. A theoretical model of an off-beam QEPAS-based sensor was proposed in Ref. [43]. By deriving the acoustic impedances of the mR at two ends and the side slit in the middle in the model, a formula for numerically calculating the optimal mR parameters of OB-QEPAS-based sensor was obtained. The model was used to calculate the optimal mR length and inner diameter with respect to the resonance frequency of the QTF as well as the acoustic velocity inside mR, finding a close match with experimental data. A low-cost UV LED has been employed as the light source in an off-beam QEPAS setup for ozone detection and a detection limit of 1.27 ppm corresponding to a NNEA parameter of 3.02×10^{-8} $cm^{-1}\cdot W/\sqrt{Hz}$ was achieved [44]. An off-beam QEPAS sensor employing an amplitude modulated, low-cost diode laser emitting at 450 nm was realized for NO_2 detection. The detection limit (3σ) was determined to 1.8 ppb using a lock-in integration time of 20 s, corresponding to a NNEA of 2.5×10^{-8} $cm^{-1}\cdot W/\sqrt{Hz}$ [45]. Hydrogen sulfide trace gas detection based on off-beam QEPAS using a CW, mode-hop-free external cavity QCL (EC-QCL) tunable from 1310 to 1210 cm^{-1} was reported in Ref. [46]. A 1-σ MDL of 492 ppb using a 1-s lock-in time constant was obtained by targeting the line centered at 1234.58 cm^{-1} (NNEA of 3.05×10^{-8} $cm^{-1}\cdot W/\sqrt{Hz}$).

15.3.2 Fiber-coupled

One of the critical issues of a QEPAS sensing system is the optical alignment. Efficient QEPAS sensors require a good laser beam quality with circular symmetry, as close as possible to the fundamental transverse TEM_{00} mode and a diffraction-limited low beam divergence with M^2 values in the range 1.0–1.3. Different approaches, starting from a standard solution based on focusing lenses, have been implemented to focus the laser light between the QTF prongs and through the mR avoiding that the laser beam illuminates the ADM. The use of a pinhole to filter out beam tails becomes necessary for laser beams with poor spatial quality. In this case, an aspheric lens focuses the laser beam through a pinhole and then collimating optics collects the light passing through the pinhole. However, spatial filters reduce the optical power focused through the QTF

and consequently reduce the QEPAS signal. An effective solution for improving the mid-IR laser beam profile is the use of single-mode optical fibers. Single-mode fiber can act as efficient modal filters and they have been implemented in QEPAS-based sensors. Compact, versatile and flexible QEPAS sensors with simple optical alignment have been realized by employing a single-mode fiber delivery system of a near-IR laser source and the ADM [47, 48]. The extension of this approach to mid-IR QEPAS sensors is limited by the lack of low-loss, single-mode optical fibers. Solid core fibers have been demonstrated to be efficient for mid-IR beam single-mode delivery using both ICL [49] and QCL [50] as light sources. However solid core fiber operation becomes multimode at wavelength λ>4.5 µm and hollow core waveguides (HCWs) represent the only solution for longer wavelengths. In HCWs the laser beam propagates through an air core by multiple reflections on a metallic inner wall [51]. The main advantages of HCWs are a high-power threshold, low insertion loss, no-end reflections, and low beam divergence at the waveguide exit. In addition, the waveguide core is coated with a dielectric film having a thickness chosen to minimize waveguide transmission losses in the metallic layer at the wavelength of the propagating laser radiation [52]. The overall loss and spatial mode properties are mainly determined by the bore size d. A single-mode Gaussian-like beam profile output can be obtained when $d<30\,\lambda$. However, for practical applications a small bore size is not always desirable, since the smaller the bore size, the greater the loss, which scales as $1/d^3$ [53]. For laser wavelengths near λ~10 µm, a 300-µm bore fiber offers a good compromise by providing single-mode beam delivery with low transmission losses [54–58]. Spagnolo et al. developed a QEPAS sensor system using a HCW-coupled single-mode QCL light source [59]. A scheme of the fiber-coupled QEPAS sensor is depicted in Fig. 15.6B. Single-mode laser delivery was obtained using a HCW with inner silver-silver iodine (Ag-AgI) coatings, an internal bore size of 300 µm, with transmission losses of 1 dB/m and bending losses of 0.1 dB [32]. The EC-QCL output beam must be mode-matched to optimally couple into the ~0.04 numerical aperture of the HCW. A ZnSe lens with a 12.7 mm diameter and 40 mm focal length was selected to ensure a focused spot diameter of <300 µm in order to maximize the laser light delivered by the HWG to the QTF. A beam waist diameter of ~160 µm was measured in the focal plane of the focusing lens, which is well below the gap width of the QTF prongs. Hence, 99.4% of the laser light exiting from the collimator was transmitted through the ADM without touching it and allowing a strong reduction of the background finger-like pattern in QEPAS spectra. The fiber-coupled QCL-QEPAS system was then tested by employing a 10.54-µm external cavity QCL (EC-QCL) with an output power of up to 90 mW and choosing SF_6 as the target gas. A SF_6 absorption line located at 948.615 cm^{-1} was selected, which is free from water interference. For a 1-s lock-in integration time a minimum detection sensitivity of 50 ppt was achieved, corresponding to a NNEA=2.7×10^{-10} $cm^{-1}\cdot W/\sqrt{Hz}$, which represents a record value for the QEPAS technique. A fiber-coupled QEPAS sensor has also been reported by Siciliani de Cumis et al. [60]. A single-mode HWG with inner silver-silver iodine (Ag-AgI) coatings and internal core diameter of 200 µm was optically coupled with an EC-QCL operating in 7.6–8.3 µm spectral range. In this case, an output focuser was specifically designed to provide a beam size and waist small enough to be focused through the mR tubes and between the 32.7 KHz QTF prongs without hitting them.

The sensor was tested for detection of H_2S, a molecule of high interest for environmental monitoring due to its high toxicity. The fiber-coupled QEPAS sensor reached a detection limit of 3 ppm of H_2S in N_2. The sensitivity was improved by ~1 order of magnitude (330 ppb) by increasing the integration time up to ~30 sec, 1.5 times better than the result obtained in the near-IR at 2.64 μm [61].

15.3.3 Evanescent-wave

As discussed in the previous section, precise collimating/focusing optics or fiber-coupling systems minimizing the optical insertion loss and improvements of the efficiency of QEPAS signal generation are usually employed. An alternative approach is the use of tapered optical micro/nanofibers to generate evanescent waves for the photoacoustic generation. Fiber tapers with diameters down to the sub-wavelength scale and low loss of ~0.2 dB can be fabricated by using a flame-brushing technique starting from standard single-mode fibers. The tapered fiber is threaded through the gap between the two QTF prongs, and thus the laser radiation is guided along the fiber with a very small beam size and hence no precise optical alignments are needed (Fig. 15.6C). The laser light is transmitted to the tapered fiber and the evanescent field is absorbed by the nearby target gas, generating an acoustic pressure wave that is detected by the QTF. Calculations based on the finite element method have shown that, when operating at 1.5 μm, as the fiber diameter is reduced to <1 μm, the percentage of the evanescent field in air increases rapidly. When the diameter of fiber is 0.6 μm, >80% of the light power will be in the evanescent field, which enables an efficient interaction between the sensing gas and the laser source [62]. The evanescent-wave QEPAS configuration was first reported in 2012 by Cao et al. They employed a fiber taper of a 1.1-μm waist diameter, a bare 32.7 kHz QTF and a DFB laser with a wavelength of 1.532 nm. With 9.8 mW output optical power used as the light source results in an MDL of 178 ppm for C_2H_2 detection at atmospheric pressure, corresponding to a NNEA=1.96×10^{-6} $\mathrm{cm^{-1}\cdot W/\sqrt{Hz}}$ [63]. In 2017, Ren et al. proposed an evanescent-wave QEPAS sensor for CO detection with the fiber taper inserted through the two mR tubes (OB configuration) with the taper waist located between the QTF prongs [64]. A fiber-coupled CW DFB laser emitting at 2.3 μm was connected with the fiber taper fabricated by the flame-brushing method. Ren et al. showed that the fiber taper has negligible influence on the resonant frequency and Q-factor of the QTF, but significantly reduces the background noise. The developed CO sensor achieved an MDL of ~20 ppm, corresponding to a NNEA of 1.44×10^{-8} $\mathrm{cm^{-1}\cdot W/\sqrt{Hz}}$, two orders of magnitude better than the previous evanescent-wave QEPAS demonstration by Cao et al. This approach provided an alternative to the general open path-based QEPAS technique, having advantages of lower insertion loss, easier optical alignment and multiplexed trace gas-sensing capability.

15.3.4 Multi-QTFs

The theoretical and experimental investigation of the mR position along the QTF axis discussed in Section 15.2.2 showed that a QEPAS signal-to-noise plot as a function of the mR vertical position shows a maximum centered on a nearly flat curve [65].

This flat curve region is sufficiently wide, which allows the positioning of two mRs in a QTF. This novel QEPAS configuration has been referred to as "double mR QEPAS" [66] and is schematically depicted in Fig. 15.7A. The lowering of the ADM Q-factor due to the acoustic coupling of the QTF with the two mRs leads to an ADM response time 20 times faster compared with a bare QTF and to a wider response bandwidth. Hence, the signal amplitude and phase of the double mR spectrophone become insensitive to small drifts of the resonant frequency compared to the high-Q bare QTF and single mR spectrophone. This can extend the calibration time interval of the QEPAS sensor system. However, the double mRs coupled to the QTF adds a dissipation channel of the vibrational energy of the QTF so that a part of signal amplitude is lost. Thus, the double AmR spectrophone sensitivity is usually five times less than that of the single mR spectrophone. Such a double mR configuration can provide two advantages: (i) two laser excitation sources from different optical wavelength can perform the optical signal addition or cancellation by means of the spectrophone, and

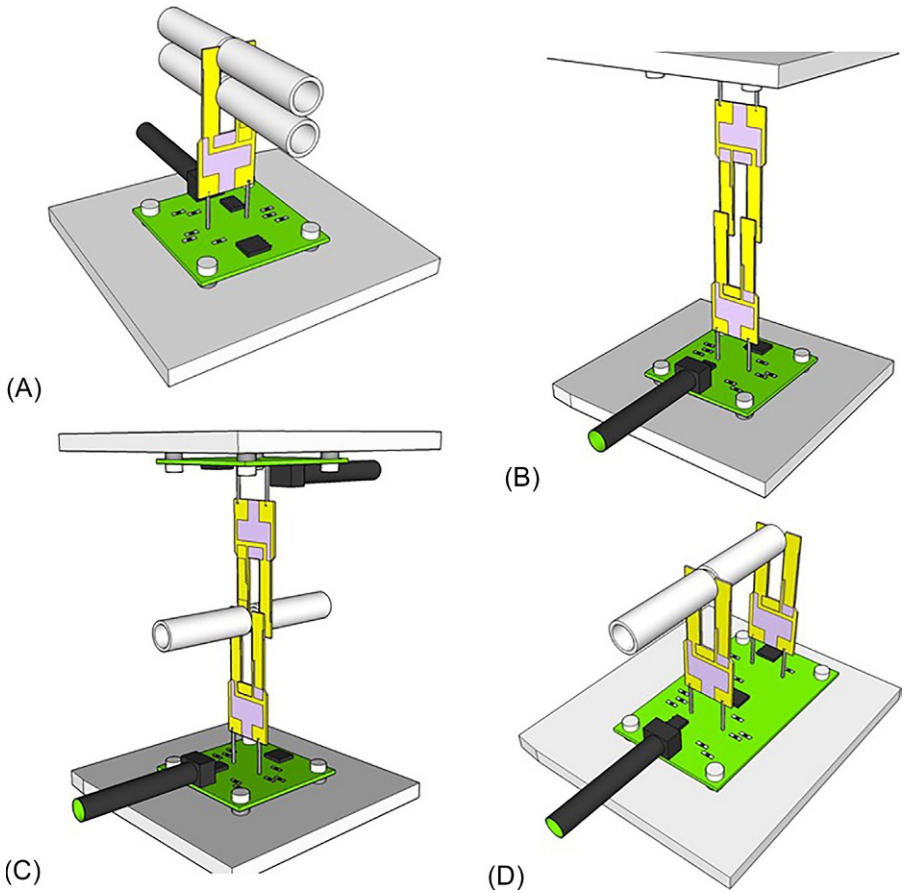

Fig. 15.7 Schematic of double mR QEPAS (A), M-QEPAS with bare QTFs (B), and M-QEPAS employing a pair of mR tubes, in two different configurations (C, D).

(ii) the spectrophone can implement ultrafast two-gas measurements by switching between two detection channels. Performing a two spectra signal cancellation with the line-locked mode of two lasers at a specific concentration ratio of two target gases, the double mR spectrophone is able to measure directly the deviation of the concentration ratio. The deviation can then be used as a feedback to control gas valves in order to maintain a specific gas mixing ratio, which is important for controlling gas chemical reactions, gas mixtures or optimizing combustion processes.

Another configuration relies on the use of two QTFs in a single ADM [66]. In this multi-QEPAS (M-QEPAS) sensor system, the acoustic wave is simultaneously detected by multiple QTFs (Fig. 15.7B) and single QTFs signals are added to each other in order to increase the overall signal amplitude. Compared with QEPAS sensor using a bare single QTF, M-QEPAS employing two bare QTFs provided a signal enhancement of 1.7 times, with the same operating conditions. Further improvement in detection sensitivity of the M-QEPAS configuration was achieved by employing acoustic mR tubes for both QTFs [67]. Two configurations of multi-QTF in "on-beam" QEPAS system were realized [68]. When two QTFs were placed close to each other and coupled with two mRs, as shown in Fig. 15.7C, the Q-factor of the multi-QTFs system becomes higher than that of each QTF in a standard OB configuration. This configuration yielded a 1.4 times enhancement compared to the traditional single QTF-based OB configuration and an enhancement ×33 compared to the single bare QTF. For the configuration shown in Fig. 15.7D, two QTFs were spaced by one of the mR tubes. In this case, the Q-factor increases with respect to the two QTFs in a "standard" OB configuration. The QEPAS signal is 1.6 times higher than that of the traditional single QTF with a mR in OB configuration and 36 times higher than that of the single bare QTF. The signal enhancement can be further improved by using a phase shifter to adjust the phase difference among multi-QTFs and a capacitance in series with one of the QTFs to perfectly match the resonance frequencies. To enhance the acoustic signal of a QEPAS sensor, a right-angle prism was used to invert the incident laser beam and force it to pass two times through the gap between two QTF prongs [69]. Correspondingly, two pairs of rigid metal tubes were used as acoustic resonators with resonance enhancement factors of 16 and 12, respectively. The QEPAS signal was enhanced by a factor of 22.4 compared with the bare QTF signal, which was acquired without resonators or a prism.

15.3.5 Modulation cancellation method

Another effective method for reducing or cancelling the background noise generated by portion of the laser beam hitting the ADM can be accomplished by the modulation cancellation method (MOCAM). MOCAM is a variation of modulation spectroscopy using two light sources [70–72]. The basic concept of MOCAM is that the powers and modulation phases of two light sources can be adjusted to balance out the background signal, especially that caused by the stray light, which limits the measurement accuracy. MOCAM can detect a small signal in the presence of a large background noise by physical cancellation of the sensor response. Different approaches have been demonstrated for MOCAM. In a configuration to demonstrate trace gas detection of

broadband absorber species by use of wide stripe diode lasers [70], a balance laser source, whose emission wavelength is located outside the target gas absorption band is used in order to intentionally generate an identical background noise to that caused by the exciting laser source with an emission wavelength falling within the absorption band of the target gas. A schematic of this approach is shown in Fig. 15.8A.

If the two lasers are modulated in counterphase, the QTF prongs are forced to vibrate in opposite direction by the two laser sources and as a result no QTF vibrations are produced and thereby not generating a background noise signal. Other applications for MOCAM include measurements of small temperature difference in a gas mixture [71] and analysis of isotopic composition [72]. For these types of measurements, the

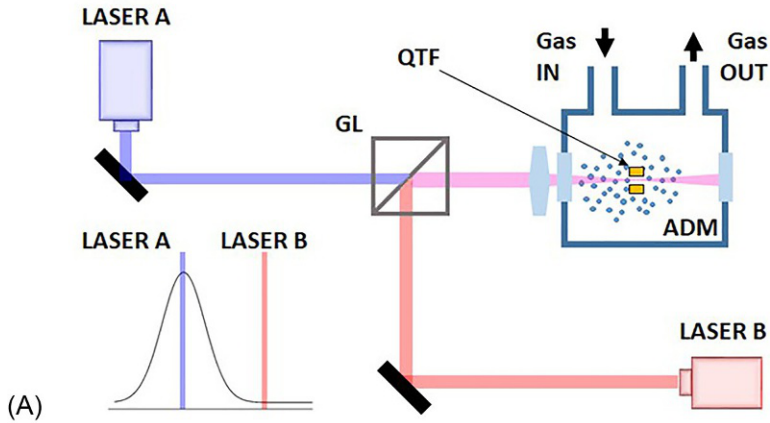

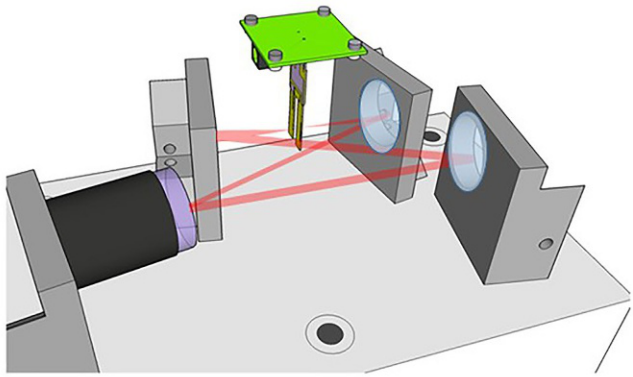

Fig. 15.8 (A) Schematic of the MOCAM approach for the detection of broadband absorbers. GL, Glenn Prism. Two laser sources are used for cancellation of the background noise: one locked to the absorption peak, while a second source is tuned far from the absorption band. (B) Schematic of the I-QEPAS configuration. A QTF is inserted within a bow-tie cavity composed of two flat and two concave high-reflectivity mirrors.

output powers and modulation phases of the two lasers resonant with two selected absorption lines are adjusted in such a way that the signal detected from the reference sample is zero. Then, in an appropriately designed optical configuration, the signal from the analyzed sample will be proportional to the deviation of the absorption line strength ratio from the reference sample line strength ratio. A variant of MOCAM was the implementation of an electrical driving signal to induce opposite QTF vibrations with respect to those generated by the exciting laser source. This approach is called electronic MOCAM (E-MOCAM). The E-MOCAM method makes it possible to use commercial high-power LEDs [73] or fiber-amplified near-IR sources [74, 75], characterized by limited beam qualities as excitation sources in OB-QEPAS sensors, by suppressing the background noise caused by stray light by up to three orders of magnitude.

15.3.6 Beat frequency QEPAS

The QEPAS signal is proportional to the QTF resonance Q-factor, which is related to resonator integration time by the relation $\tau_r=Q/\pi f_0$, when fast energy relaxation rates are assumed for the gas target. At low pressures, $\tau_r>1$ s can be reached for bare QTFs and is reduced to a few hundreds of milliseconds when a mR system is used [19]. In order to allow the acoustic mode of the resonator to accumulate all the absorbed laser energy, the QEPAS signal integration time should be 3–4 times longer than τ_r, which means a few hundreds of milliseconds for uncorrelated trace gas concentration measurements. Such integration time values are suitable for applications requiring no fast changes in the gas sample composition, which are expected in short time intervals. However, such integration times are too long for rapid scan trace gas measurements required for applications like multiline detection of the same or different gas species, where scan rates >1 Hz are usually required [76]. A recent and innovative QEPAS technique approach relying on beat frequency (BF) signals between the QTF resonance frequency f_0 and the laser modulation frequency was reported in Ref. [77]. The BF-QEPAS concept requires that the laser modulation frequency differs by Δf_B with respect to the QTF resonance frequency f_0. For this condition, a BF-QEPAS signal with a period of Δt_B is generated when the laser wavelength is rapidly scanned across a targeted absorption line and the QTF signal is demodulated at the same frequency f. In BF-QEPAS, an acoustic pulse induced by the target gas absorption is generated, which causes the prongs of the QTF to vibrate in a short period of time. Subsequently, while the QTF relaxes the accumulate energy at its natural mode frequency via loss mechanisms and the QTF signal is demodulated at the laser modulation frequency f. When the averaging time is short enough (<100 ms) to provide a sufficient system detection bandwidth, a BF signal with an exponential decay envelope is generated from the QTF-transient response. The concentration of the trace gas, the resonance frequency and Q-factor of the QTF can be obtained by measuring the amplitude of the envelope, Δt_B and the decay time τ_c of the BF-QEPAS signal, respectively, all in a measurement time as short as a few tens of milliseconds. Such a method provided a comparable detection sensitivity with respect to conventional QEPAS, when fast-relaxing molecules such as H_2O are detected. It should be noted that the BF-QEPAS technique can be employed in any QEPAS-based sensor systems without any hardware changes of a conventional QEPAS ADM system.

15.3.7 Intracavity QEPAS

The intensity of the QEPAS signal is directly proportional to the power absorbed by the target species (see Eq. 15.4) and thus the sensitivity varies linearly with laser power. An increase of the optical power focused between the QTF prongs improves the MDL of a QEPAS sensor. Up to 1 W of optical power has been used for QEPAS sensing [78]. One alternative way to increase the laser power can be achieved by the employment of power build-up approaches, like the one occurring in high-finesse optical cavities. The first demonstration of a QEPAS sensor exploiting a high-finesse optical power build-up cavity was reported in Refs. [79, 80]. This novel QEPAS approach combines QEPAS technique with CEAS and was called intracavity QEPAS (I-QEPAS). A bow-tie optical resonator composed of two concave mirrors and two plane mirrors was employed. The QTF was positioned at the cavity waist between the two concave mirrors, as shown in Fig. 15.8B. The laser wavelength has to be matched with one of the cavity resonances, and a proper locking between the laser frequency and the cavity resonance was implemented for spectral scans. By using a closed-locking loop electronic circuit, it was possible to force the laser and the cavity to be in resonance by adjusting the cavity length with a piezoelectric actuator attached to one of the cavity mirror. In this way, the laser was kept in resonance with the cavity length and a high spectral resolution was achieved. The effective intracavity power enhancement factor strongly depends on the cavity finesse and on the quality of the mode matching between the laser and the cavity. This can be optimized by appropriately handling of the beam geometry entering the cavity and by using laser radiation with a linewidth comparable to, or narrower, than the cavity mode. In addition, the laser mode must match as well as possible the TEM_{00} cavity in order to have an intracavity beam with an excellent spatial beam profile, which is advantageous for proper focalization of the beam between the QTF prongs. With mirror reflectivities >99% and a cavity length of 174 mm, a cavity mode FWHM of 1.15 MHz was measured, with a bow-tie cavity finesse of 1505 [79]. A CW quantum cascade laser emitting at 4.33 μm was used in combination with a low-noise stabilized current source, reaching a laser linewidth <1 MHz. CO_2 detection with an MDL of 300 ppt was achieved with an integration time of 20 sec, corresponding to a NNEA of 3.2×10^{-10} $cm^{-1}\cdot W/\sqrt{Hz}$. The improvement in terms of sensitivity with respect to conventional QEPAS setup (operating under the same conditions of molecular linewidth, pressure, and laser output power) was demonstrated to be equal to the power enhancement factor occurring in the optical resonator (~240 in Refs. [79, 80]). Hence I-QEPAS is one of the most sensitive cavity-based techniques, similar to ICOS or CRDS. Recently, a novel compact bow-tie cavity capable to reach power enhancement factors over 300 has been realized [81], promising even further improvements in detection sensitivity. Moreover, since a bare QTF was used as an ADM in the first I-QEPAS demonstration, further improvements are feasible by adding a mR tube system to the ADM located in the optical cavity. The first I-QEPAS demonstration showed that efficient coupling of the laser beam into the external optical cavity requires a narrow laser linewidth and full overlap of laser frequency with the cavity transmission mode. Hence, to fully exploit the laser power enhancement, the sensing element can be positioned directly inside the laser cavity.

This concept yielded a fiber-ring laser intracavity QEPAS (FLI-QEPAS) [82]. The sensor implements a QTF positioned inside a fiber-ring laser cavity. A CW fiber-ring tunable laser was developed using a fiber Bragg grating (FBG) to target the C_2H_2 absorption line located at 1531.6 nm. The small size of the acoustic cell containing the bare QTF allowed a short-path intracavity gas absorption length (1.5 cm), leading to a reduction of cavity losses induced by gas absorption. A FBG-based modulator was designed to modulate the intracavity laser wavelength at half of the QTF resonant frequency, while maintaining the intracavity laser power constant over the entire wavelength scanning range. The FLI-QEPAS sensor achieved an MDL of 29 ppb for C_2H_2 detection in N_2 with a lock-in integration time of 300 sec.

15.4 Custom QTFs for QEPAS

Since its introduction in 2002 and for more than 10 years later, standard low-cost QTFs with resonance frequencies at 32.7 kHz have been only employed in QEPAS sensors. The light source is focused between QTF prongs and sound waves produced by the modulated absorption of the gas are generated between the QTF prongs, forcing them to oscillate back and forth (in-plane antisymmetrical flexural modes). The main problem in the realization of a QEPAS sensor is the focalization of the laser beam within the 300 μm gap between the standard 32.7 kHz QTF prongs without touching both mR tubes and the QTF itself. As already discussed, this is crucial in order to avoid the generation of a photothermal noise contribution which would be added to the piezoelectric signal [32]. When laser modulation occurs at one of resonance frequencies of in-plane piezoelectrically active modes, the induced strain field generates surface electric charges proportional to the intensity of the sound waves incident on the QTF prongs. When the light is periodically absorbed by the gas, the energy excess is mainly dissipated through nonradiative relaxation processes, involving vibrational and rotational excited states. Sound waves are then generated via energy transfer from excited states to translational degrees of freedom. The ability of the gas target to periodically relax the excess of energy depends on the modulation frequency (i.e., the resonance frequency of the QTF in-plane mode) of the incident laser radiation and differs for each gas [22, 83]. For slow relaxing gases, such as CO, CO_2, and NO a QEPAS sensor operational frequency as high as 32.7 kHz can limit the sound wave generation efficiency [19]. Thereby, these considerations suggested directions for the realization of improved custom QTFs providing (i) a reduction of the QTF fundamental frequency and (ii) an increase in the prong spacing in order to facilitate the optical alignments and minimize the photothermal noise level.

15.4.1 Euler-Bernoulli model

The resonance frequencies of a QTF flexural mode can be calculated in the approximation of an independent cantilever vibrating in the in-plane modes. Each prong of the tuning fork can be treated as a clamped beam. Assuming that two beams have an

elastic response that when an applied force is removed will return to their original shape. According to the Euler-Bernoulli approximation, the description of the vibration is given by the following fourth-order differential equation [26, 39]:

$$EI_M \frac{\partial^4 x}{\partial y^4} + \rho LT \frac{\partial^2 x}{\partial t^2} = 0 \tag{15.10}$$

where E and ρ are the Young Modulus and the volume density of quartz, respectively, L and T are the prong length and thickness, respectively, I_M is known as second moment of beam's cross-sectional area and x and y are the directions in the QTF plane (see Fig. 15.3A). The product EI_M is usually referred as the flexural rigidity. The flexural rigidity, the cross-sectional area LT and the volume density are assumed to be constant along the whole beam. The Euler-Bernoulli equation can be solved by the separation of variables method. The displacement can be separated into two parts, one depending on position and the other one is a function of time. This leads to a simplified differential equation for the x direction that can be solved by superimposing boundary conditions. The boundary conditions originate from the support of the QTF. The fixed end must have a zero displacement and zero slope due to the clamp, while the free end does not have a bending moment or a shearing force (free-clamped boundary conditions). The general solution is a linear combination of trigonometric equations leading to the following equation for the cantilever beam: $\cos(k_nL)\cosh(k_nL) = -1$, where k_n are the wavenumbers (k_0=0.11 mm^{-1} and k_1=0.28 mm^{-1} for the fundamental and first overtone mode, respectively) related to the Eigen frequencies f_n, given by the following expression:

$$f_n = \frac{\pi T}{8\sqrt{12}L^2}\sqrt{\frac{E}{\rho}}\upsilon_n^{\,2} \tag{15.11}$$

where ν_n identifies the mode number, i.e., n=0 identifies the fundamental flexural mode, n=1 the first overtone mode, n=2, the second overtone mode, and so on. The first four ν_n values are reported in Table 15.1.

The Euler-Bernoulli theory allows also the estimation of the mode shape of the displacement x along the y-axis as function of the distance from the prong base, given by Eq. (15.12) [84]:

$$x(y) = A_n \left\{ \left[\cosh(k_n y) - \cos(k_n y)\right] + \left[\frac{\sin(k_n L) - \sinh(k_n L)}{\cos(k_n L) + \cosh(k_n x)}\right]\left[\sinh(k_n y) - \sin(k_n y)\right] \right\} \tag{15.12}$$

Table 15.1 ν_n values calculated by solving the cantilever beam equation $\cos(\boldsymbol{K_nL})\cosh(\boldsymbol{K_nL}) = -1$.

N	ν_n
0	1.194
1	2.988
2	5
3	7

where A_n is the vibration amplitude for the nth vibrational mode. The model predicts $n+1$ node points and $n+1$ antinode points for the nth flexural mode. The fundamental mode has one antinode point on the top of prongs. For the first overtone mode, the first antinode point is on the top of the prong, while the second one is close to its center. With respect to the predicted positions, the vertical position of the focused laser beam maximizing the QEPAS signal for the antinode point on the top of prongs is always downshifted in agreement with the simplified model proposed in Ref. [19]. This discrepancy results from the spherical symmetry of the exciting acoustic wave. The closer to the prong top is the vertical position of the acoustic source, the larger is the fraction of the pressure wave not hitting the QTF prongs. When operating at the first overtone frequency, the downshift of the optimum vertical position of the laser spot for first antinode [84, 85] favors the QEPAS operation with the second antinode. Indeed, an increase of the QEPAS signal of a factor of 1.3 was observed while moving the laser spot focus from the first antinode to the second antinode.

The Euler-Bernoulli presented so far is also valid for a single cantilever. One could therefore argue that it would be sufficient to use a cantilever quartz beam of the size of the fork's prong as a QEPAS sensor. However, with the same geometry involved, a QTF typically provides a Q-factor that is far superior to that of a single cantilever. This leads to an improved detection sensitivity of the QTF fork when employed in a QEPAS sensor. Indeed, a QTF is a system of two-coupled cantilever oscillating in opposition. The result is that the center of mass remains still, in spite of its prongs motion. In contrast, a resonating single cantilever beam has an oscillating center of mass. This motion dissipates energy and this channel of energy dissipation is obviously not present in a well-balanced QTF. The only channels for energy dissipations remain the internal dissipation (thermoelastic damping and support losses) and the damping caused by the interaction between the QTF and the surrounding gas. Dissipations occurring through the center of mass are generally larger than losses caused by mechanisms previously mentioned and cause a reduction of Q-factor of several orders of magnitude. This explain why a QTF is widely used for a wide range of application. An extensive study of the main loss mechanisms occurring in a vibrating prong will be discussed in Section 15.4.2.

15.4.2 Damping effects

The main loss mechanisms for a vibrating prong are due to (i) air damping, related to the transfer of energy and momentum from the QTF prongs to the surrounding medium; (ii) a support loss, related to the transfer of mechanical energy from the vibrating prong to the support; and (iii) thermoelastic damping, related to coupling between the strain field and the temperature field inside the QTF [28]. Air damping is referred to as an extrinsic loss mechanism, while thermoelastic and support damping are referred to as intrinsic loss mechanisms. Each resonance mode is characterized by a different vibration profile along the QTF axis, with antinode points identifying the position of maximum vibration amplitudes along the prong. The fundamental mode has one antinode point, while the first overtone mode is characterized by two antinode

points. Hence, the fundamental mode can be represented by a single point mass on the prong tip while the first overtone mode can be modeled as two-coupled point masses oscillating in counterphase [85]. In other words, each vibrational mode is expected to exhibit a different quality factor because loss mechanisms are also dependent on the related vibrational dynamics.

15.4.2.1 Air damping

When a QTF vibrating prong is immersed in a fluid, a drag force is exerted on it. This force is proportional to the local velocity of the prong in terms of a damping parameter C_f. The knowledge of the damping parameter allows calculations of the mechanical quality factor of the damped system. Since C_f is pressure-dependent, the pressure range from vacuum to atmospheric pressure is usually divided into three regions: an intrinsic, a molecular and a viscous region, each characterized by a different dominant damping mechanism [86]. In the intrinsic region, the fluid pressure is so low that the damping is negligible compared to the intrinsic damping of the vibrating beam itself. Hence, the Q-factor is independent on the fluid pressure. In the molecular region, the damping is caused by independent collisions of noninteracting molecules with the vibrating beam. In this case, the drag force can be determined by employing the kinetic theory of gases, leading to a damping parameter C_f proportional to the fluid pressure and the beam geometry. In the viscous region, the medium acts as a viscous fluid and the drag force is calculated using fluid mechanics [87]. W. E. Newell [88] derived an expression for the critical pressure p_c where the air damping changes from that typical of a molecular region to that typical of a viscous region, p_c=0.3 torr/w, where w is the crystal width expressed in millimeters. With 0.25<w<0.5 mm, which is the typical range for QTFs for QEPAS, p_c is <1.2 torr. Hence, QTFs operate in the viscous region. When the QTF undergoes harmonic oscillations of small amplitude in a fluid, the Euler-Bernoulli equation can be modified by adding a resistive term (which leads to energy dissipation by acoustic losses) and a reactive term (which leads to the additional inertia of the QTF) [89]. Starting from these assumptions, Blom et al. [86] derived an analytical expression for both the total mechanical energy of the vibrating beam and the dissipated energy per period, leading to a formulation of the quality factor related to fluid damping (Q_{air}):

$$Q_{air} = \frac{2\pi\left(\rho T w + u\right) f_n}{C_{air}} \tag{15.13}$$

where u is the added mass per unit length. Q_{air} does not depend on the vibrating mode shape and for this reason this expression can be applied to each vibrational mode, provided the damping parameter is known. Hosaka et al. [90] have proposed an approximation for the air damping problem of a vibrating prong. They considered each prong of the QTF with a rectangular cross section as a string of spheres [91]. If these spheres vibrate independently of each other, the resulting drag force is the sum of the drag force of single spheres. Starting from this approximation, they made two assumptions: (i) the length L of the QTF prong is much greater than its thickness T and crystal width w, and (ii) every single portion of the beam is replaced with a sphere

of diameter equals to w. Hosaka et al. derived an expression for C_{air} and a formulation of Q_{air} given by:

$$Q_{air} = \frac{4\pi\rho T w^2 f_n}{3\pi\mu w + \frac{3}{4}\pi w^2\sqrt{4\pi\rho_{air}\mu f_n}} \tag{15.14}$$

where ρ_{air} is the air density and μ its viscosity. Losses due to the air damping, proportional to the reciprocal of Q_{air}, consists of two terms: one pressure-independent (assuming a negligible dependence of f_n on the air pressure) and the other one pressure-dependent. The Q_{air} depends on the air pressure as well as the resonance frequency and the prong sizes. In Fig. 15.9A, Q_{air} is plotted as a function of the pressure considering a QTF having L=11 mm, T=0.5 mm and w = 0.25 mm, for both the fundamental and the first overtone mode (μ=1.81×10^{-5} kg/m·s). ρ_{air}=MP/R_CT_e is estimated by using the ideal gas law, where M=28.964 kg/mol is the molar mass, R_C=62.3637 m^3 torr/K·mol is the gas constant and T_e (in K) is the prong temperature.

In both cases, Q_{air} decreases rapidly when the pressure increases from 25 to 150 torr. At higher pressures, Q_{air} levels off and becomes quasi-asymptotic at atmospheric pressure. The air damping mechanisms are strongly reduced for higher order vibrational modes. By combining Eqs. (15.11) and (15.14), an explicit dependence of Q_{air} can be derived as a function of the prong size. In Fig. 15.9B, Q_{air} is plotted as a function on the ratio T/L, in which L ranges from 3 mm to 17 mm and 0.2<T<1.4 mm, for w=0.25 mm. The data were simulated at an air pressure of 50 torr. For a fixed pressure and crystal width, a quasi-linear dependence of Q_{air} on the ratio T/L is observed. The guideline that emerges from this model is that to reduce viscous losses, the T/L ratio must be kept high. In addition, the lower the crystal thickness, the higher the air damping losses.

15.4.2.2 Support losses

Although the history of support losses can be tracked back to the 1960s, this field still requires improved models to quantify these types of energy dissipations. Models describing support losses are developed using the theory of elasticity taking into

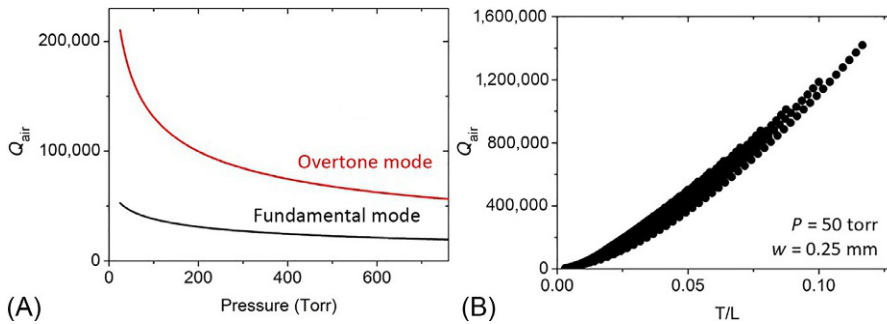

Fig. 15.9 (A) Q_{air} plotted as a function of the gas pressure for a QTF with a prong length and width of 11.0 and 9.5 mm, respectively, and a crystal thickness of 0.25 mm for the fundamental (*solid black curve*) and the first overtone (*solid red curve*) mode. (B) Q_{air} plotted as a function of the ratio between prong thickness T and its length L for a crystal thickness w=0.25 mm at an air pressure of 50 torr.

account the beam dynamics and stress wave propagation [92–95]. Several models have been developed to analyze support loss and all of them share the following set of assumptions: (i) elastic waves are transmitted to the support because of the vibrating shear forces induced by the oscillating beam with a fixed end, (ii) energy propagating through the support does not reflect back into the resonator, and (iii) the prong support junction section is assumed to have zero displacement. The simplest model was developed by Hao et al. [94], in which the prong is supposed to be a rectangular cross-section resonator, attached monolithically to a large support with the same thickness as that of the prong. The crystal thickness w is assumed to be much smaller than the elastic wavelength of the propagating waves. The closed-form expression for the quality factor related to the support loss in a clamped-free cantilever can be expressed as:

$$Q_{\text{sup}} = B_n \frac{L^3}{T^3} \tag{15.15}$$

with A_n coefficients depending on the resonance mode number and the prong material. Hao et al. [94] estimated B_0=2.081 for the fundamental mode and B_1=0.173 for the first overtone mode. Other models were developed, all of them agreeing on the support losses $(L/T)^3$ dependence, but differing in coefficient values [92, 93, 95]. From these models, the straightforward approach for reducing support losses is designing QTFs having prongs with large length-to-thickness aspect ratios. In addition, higher order modes suffer higher support losses, according to Ref. [94]. An increase of a factor of ~12 on support losses is expected for a QTF, when changing from the fundamental to the overtone mode.

15.4.2.3 Thermoelastic damping losses

Thermoelastic dissipation is an intrinsic structural dissipation mechanism of the oscillating elements, which can be expressed using a modeling approach proposed by Zener [96]. The physical explanation for this dissipation mechanism is based on the coupling between the strain and the temperature fields. Energy dissipation comes from an irreversible heat flow due to the local temperature gradient that accompanies the strain field. The following equation calculates the quality factor Q_{TED} related to the thermoelastic loss for an isotropic homogeneous beam:

$$Q_{TED} = \frac{\rho c_T}{E\beta_T^2 T_e} \frac{1+\left(\frac{2c_T f_n \rho T^2}{\pi\lambda_T}\right)^2}{\frac{2c_T f_n \rho T^2}{\pi\lambda_T}} \approx \frac{2c_T^2 \rho^2 f_n T^2}{\pi\lambda_T E\beta_T^2 T_e} \propto \frac{T^3}{L^2} \tag{15.16}$$

where λ_T, c_T, and β_T are the thermal conductivity, the heat capacity per unit mass and the thermal expansion of the prong, respectively. By combining Eqs. (15.11) and (15.16) in a first approximation, Q_{TED} scales with prong size as T^3/L^2. In addition, thermoelastic damping decreases as the resonance mode number increases, which implies that the fundamental mode is the most affected by this type of loss mechanism.

15.4.3 Quality factor

All loss mechanisms described in the previous section strongly depend on the QTF prong size. Theoretical models describe the dependence of each loss mechanism on the geometry of the prongs as a standalone. There is no theoretical model capable to take into account all the dissipation mechanisms in one consistent formulation. However, since the dissipation mechanisms are assumed independent of each other and the resonator quality factor is proportional to the inverse of total energy dissipated, the overall Q-factor can be represented as a reciprocal sum of independent dissipative contributions:

$$\frac{1}{Q(P)} = \frac{1}{Q_{air}(P)} + \frac{1}{Q_{\text{sup}}} + \frac{1}{Q_{TED}} \tag{15.17}$$

Since thermoelastic and support losses are assumed to be independent to the air pressure, it is possible to define $Q(0)$ as:

$$\frac{1}{Q(0)} = \frac{1}{Q_{\text{sup}}} + \frac{1}{Q_{TED}} \tag{15.18}$$

where Q_{air} in Eq. (15.14) can be expressed as a function of gas pressure by using the general gas law:

$$Q_{air} = \frac{a_0}{b_0 + c_0\sqrt{P}} \tag{15.19}$$

Where $a_0=4\pi\rho Twf_n$, $b_0=3\pi\mu$ and $c_0=(3/4)\pi\mu w\sqrt{(4\pi Mf_n/\mu N_A KT_e)}$, since $\rho_{air}=MP/N_A KT_e$, where N_A is Avogadro's number. As defined, $Q(0)$ does not include the pressure-independent contribution derived from the Hosaka's model [90]. By combining Eqs. (15.17), (15.18), and (15.19), the overall Q-factor can be rewritten as:

$$Q_{air} = \frac{1}{A + B\sqrt{P}} \tag{15.20}$$

where $A=1/Q(0)+b_0/a_0$ and $B=c_0/a_0$. Hence, the Q-factor strongly depends on the gas mixture pressure and as a consequence the QEPAS detection sensitivity in a specific absorbing gas sample is a function of the sample pressure [28]. This dependence is also influenced by three other factors: (i) at low gas pressures the collisional line broadening of the absorption peak is less than Doppler broadening, and thus the merging of closely spaced absorption lines should be taken into account at higher pressures; (ii) V-T relaxation rates are faster at higher pressures, which is in competition with the opposite trend of the Q-factor; and (iii) the speed of sound depends on the gas pressure. This means that the optimal gas pressure enhancing the QEPAS signal is a tradeoff between these simultaneously concurring phenomena and is usually determined experimentally since there is no theoretical model to predict it.

15.4.4 Overtone modes

The feasibility to realize custom-made QTFs optimized for QEPAS applications can significantly improve the sensitivity of QEPAS ADMs. With respect to the standard 32.7 kHz QTF, the resonance frequency of the fundamental mode can be reduced to

a few kilohertz in order to better approach the typical energy relaxation time of targeted gases [26], while maintaining a high resonator quality factor. Both conditions can be simultaneously satisfied by an appropriate design of the QTF prong sizes. However, lowering the fundamental resonance frequency reduces also the overtone frequencies, leading to their investigation and use in QEPAS sensor systems. This is not feasible with a 32.7 kHz QTF, since its first overtone mode occurs at frequencies higher than 190 kHz, which is impractical for QEPAS-based gas detection. By using the Euler-Bernoulli equation, the first overtone mode exhibits a resonance frequency $2.988^2/1.194^2 \sim 6.26$ times higher than the fundamental mode. This implies that in order to have the first overtone resonance frequency <30 kHz, the fundamental mode must vibrate at frequencies lower than 4.5 kHz. Lowering the operating frequency at values <3 kHz is not recommended in QEPAS since the sensor system would be more influenced by environmental acoustic noise. The fundamental and the first overtone modes exhibit different quality factor values because the associated loss mechanisms depend on the related vibrational dynamics and on the geometry of the QTF prongs. Hence, the QTF geometry can be designed to provide an enhancement of the overtone mode resonance Q-factor and as a consequence a higher QEPAS SNR with respect to the fundamental mode can be expected. According to Hosaka's model [90], the air damping is significantly reduced when moving from the fundamental to overtone mode. For example, for a QTF having L=11 mm, T=0.5 mm and w=0.25 mm, $Q_{air,\ over}/Q_{air,\ fund} \sim 4$ (see Fig. 15.9A) at 25 torr. However, moving to higher modes, support losses can start to dominate, deteriorating the overall quality factor. An increase of a factor of ~12 on support losses is expected for a QTF, when changing from the fundamental to the first overtone mode (see Section 15.4.2.2). With respect to the fundamental mode, the Euler-Bernoulli equation predicts two antinode points for the first overtone mode shape are both suitable for QEPAS sensing. Even if the electrodes layout for charge collection is designed as a quadrupole pattern, matching the charge distribution generated by the in-plane fundamental mode vibration, the first overtone mode can be also excited. However, such an electrode configuration partially impedes the excitation of the first overtone flexural mode. An innovative electrode pattern optimizing the first overtone flexural mode charge collection by analyzing the stress field distribution along the QTF prongs was proposed by Patimisco et al. [97]. When the prongs of a tuning fork are in their natural oscillatory motion, the stress produced along the prong can be expressed by a longitudinal tensor $\sigma_p(x,z)$, where x and y identify a Cartesian plane orthogonal to the prong (aligned along the y-axis, see Fig. 15.3A). The stress induces a local polarization $p_0(x,y)$ of quartz and charges appearing on the surface can be collected by electrical contacts deposited along the QTF prong. The polarization depends on the stress field as $p_0=[d]\sigma_p$, where $[d]$ is the quartz piezoelectric tensor. Assuming that the QTF axes correspond to the quartz crystal axes and considering the effects of the polarization perpendicular to the tensile stress, the relation between p_0 and σ_p reduces to the scalar expression $p_0=-d_{11}\sigma_p$, where d_{11} is the longitudinal piezoelectric modulus. In the elastic regime, in which there is a linear relationship between the stress and strain fields, it can be shown that σ_p is proportional to the second derivative of the displacement for a bent QTF prong. By using the formulation of

the displacement derived from the Euler-Bernoulli model (see Eq. 15.12), the tensile stress along the prong axis is given by:

$$\sigma_p(y) = S_n \begin{Bmatrix} \left[-\cosh(k_n y) - \cos(k_n y)\right] + \left[\dfrac{\sin(k_n L) - \sinh(k_n L)}{\cos(k_n L) + \cosh(k_n x)}\right] \\ \left[-\sinh(k_n y) - \sin(k_n y)\right] \end{Bmatrix} \tag{15.21}$$

S_n is the stress amplitude. The curves in Fig. 15.10A–D show the distribution of both the lateral displacement and normalized strain along the prong as a function of the distance s from the prong support junction for the fundamental and first overtone mode obtained by using Eqs. (15.12) and (15.21).

The fundamental mode shows the highest stress antinode at s=0. The first overtone mode shows two stress antinode points, one negative at s=0 and one positive at s=9 mm. For the fundamental vibrational mode, the sign of the strain distribution does not change over the entire length of the QTF prong. Whereas, for the first overtone mode the strain direction changes along the length of the prong and consequently also

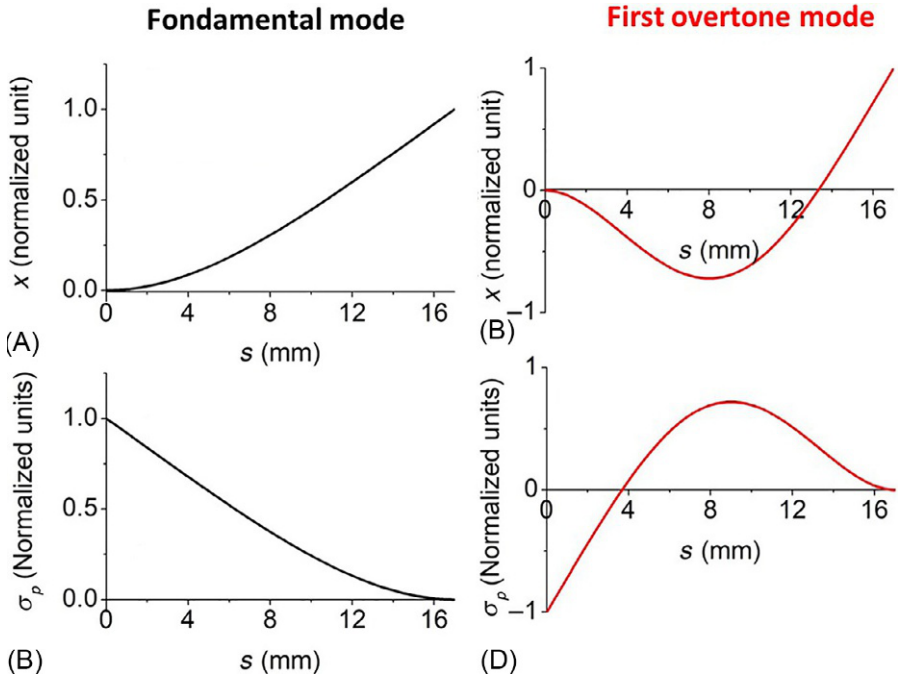

Fig. 15.10 Lateral displacement (A, B) and one-dimensional normalized stress field distribution (C, D) along the QTF prong as a function of the distance from the prong support junction for the fundamental (*black solid lines*) and the first overtone (*red solid lines*) mode. The prong length is L=17 mm.

the sign of the piezoelectrically induced charges, which reverses at the zero-stress point. The electrode patterns deposited on QTF surfaces must be divided into separated zones corresponding to opposite generated electric fields (and charges) areas in order to efficiently retrieve the piezoelectric signal provided by a specific flexural resonance mode. The separation between electrodes of different polarity is located where the sign of the strain field reverses. For the fundamental flexural mode, the sign of the stress (and thereby of the generated charges) alternates between adjacent lateral prong surfaces but remains the same along the prong length (see Fig. 15.10C). Hence, a quadrupole electrode pattern should be employed. Furthermore, for the overtone mode the sign of the stress is opposite over adjacent surfaces. Nevertheless the electrode pattern must be sectioned along the prong surface due to the presence of a zero-stress point, delimiting areas characterized by opposite stress signs and generated charges (see Fig. 15.10D). This requires a dual-quadrupole electrode layout configuration, i.e., an octupole electrode pattern for optimal charge collection. Patimisco et al. [97] realized two QTFs having the same geometry and implementing a quadrupole or an octupole electrode pattern. The prong lengths were L=17 mm and their width w=1.0 mm with a quartz crystal width of 0.25 mm. The obtained results demonstrated that employed an octupole electrode pattern configuration for a QTF vibrating in the first overtone mode, the electrical resistance decreased by a factor of ~4.4, providing a QEPAS signal ~2.3 times higher signals with respect to the quadrupole electrode pattern. In addition, the quality factor of the first overtone resonance mode was not affected by the employed contact pattern and thus the QEPAS signal amplification is determined by the charge efficiency collection, i.e., proportional to the electrical conductance. One disadvantage is that the octupole electrode layout completely suppresses the vibration at the fundamental mode, preventing its use for QEPAS measurements.

15.4.5 Overview of custom QTFs performance

With the aim of determining the dependence of the resonance frequency and the related quality factor on the relevant QTF dimensions and identify the optimal design for QEPAS, Patimisco et al. [26] designed and realized a set of QTFs with different values of spacing between the prongs, their length and thickness as well as their crystal thickness. Even if the electroelastic properties of QTFs are not influenced by the prong spacing (the two prongs can be assumed to be uncoupled), this parameter plays a crucial role in the acoustoelectric transduction efficiency, i.e., the conversion efficiency of the amplitude of the acoustic wave in the piezoelectric charge production. For a focused laser beam, in the approximation of cylindrical symmetry, the amplitude of the acoustic wave incident on the prong surface decays as $1/\sqrt{g}$ [24], with g being the distance of the QTF axis position from the internal prong surface (see Fig. 15.3A). The size of the cross-sectional area of the focused beam is determined by diffraction to the beam waist values of the order of the laser wavelength. The larger the focused beam cross area size, the larger has to be the prong spacing in order to avoid that a part of the laser radiation is incident on the QTF. For example, for near-IR laser radiation, a prong spacing <100 μm can be employed [19, 98], while for a THz laser source, it is necessary to use a prong spacing of >700 μm in QEPAS trace gas sensing [39, 99, 100].

In the mid-IR range QTFs with prong spacing of ≥300 µm have been successfully employed [19, 98]. A set of QTFs were realized starting from a z-cut quartz wafer with a 2-degree rotation along the *x*-axis, since this crystal cut provides stable flexural vibrational modes frequencies at room temperature. Furthermore, the *z*-cut is the crystal cut typically used for QTFs operating at low frequencies (up to 50 kHz). The quartz wafers were etched. A three-dimensional crystal structure is generated by chemical etching in a saturated aqueous solution of ammonium bifluoride. The temperature of the chemical etching solution was monitored directly by a temperature controller and kept at a constant 52°C. This temperature was chosen because it allows chemical etching in a reasonable amount of time while also permitting adequate control of the frequency by adjusting the etching time. A motor-driven rotary propeller provided constant agitation. The electrode pattern, consisting of chromium (50 Å thick) and gold (250 Å thick) patterns, was applied photolithographically by means of shadow masks defined on both sides of the wafer. The gap between center and side electrodes was 50 µm. A schematic of the investigated QTF set is shown in Fig. 15.11.

The quadrupole electrode layout was designed to enhance the fundamental flexural mode but also allowing all the excitation of the first overtone mode, as discussed in Section 15.4.4. The dimensions of the investigated QTFs are listed in Table 15.2.

All QTFs were tested at a pressure of 50 torr. The Euler-Bernoulli equation was used to predict the theoretical frequencies for the fundamental and the overtone modes. As an example, Fig. 15.12 shows the spectral response of QTF#2 at the fundamental and first overtone mode at a pressure of 50 torr.

In Table 15.3, the extracted values for the resonance frequencies f_0 (fundamental mode) and f_1 (first overtone mode) at 50 torr are reported and compared with the predicted values of $f_{0,th}$ and $f_{1,th.}$ Measured quality factor values for the fundamental (Q_0) and first overtone (Q_1) mode are also listed.

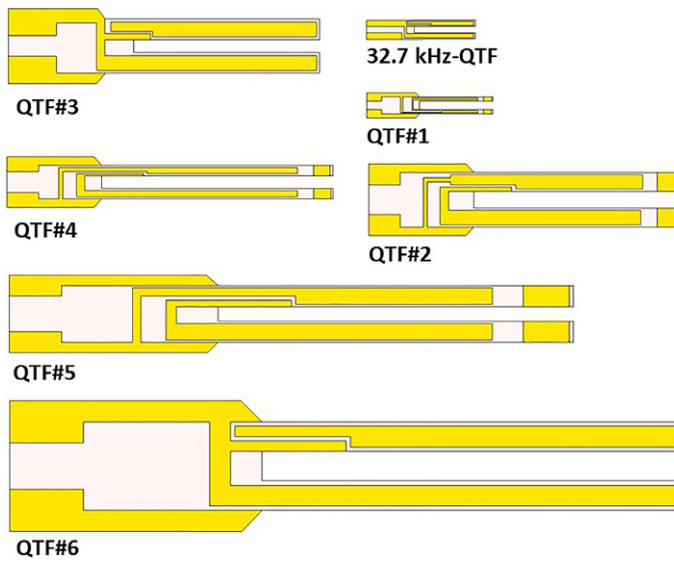

Fig. 15.11 *x–y* plane view of standard, 32.7-kHz, and custom QTFs.

Table 15.2 Dimensions of prongs of the standard, 32.7-kHz, and custom tuning forks.

	32.7 kHz QTF	**QTF#1**	**QTF#2**	**QTF#3**	**QTF#4**	**QTF#5**	**QTF#6**
L (mm)	3.0	3.5	10	10	11	17	19
W (mm)	0.35	0.25	0.25	0.5	0.25	0.25	0.8
T (mm)	0.35	0.2	0.9	1.0	0.5	1.0	1.4
$2g$ (mm)	0.3	0.4	0.8	0.5	0.6	0.7	1.0

L, QTF prong length; T, thickness of the prong; w, thickness of the quartz crystal; $2g$, spacing between prongs.

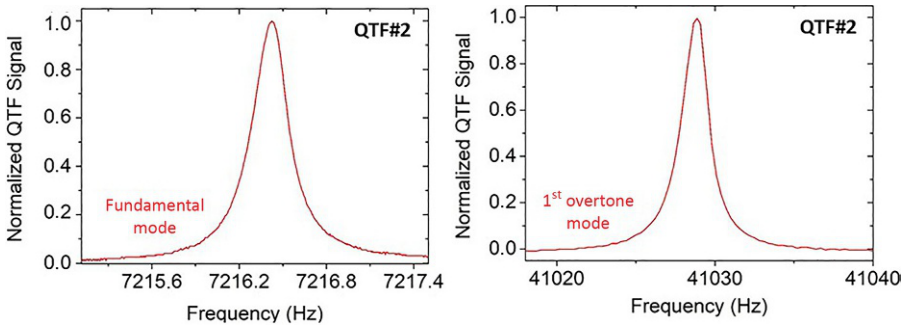

Fig. 15.12 Resonance curves of QTF current measured at a fixed excitation level and at a pressure of 50 torr in standard air, for custom QTF#2 near the fundamental mode (A) and the first overtone mode (B).

Table 15.3 Resonance frequencies measured for the fundamental (f_0) and first overtone mode (f_1).

	Fundamental mode		**First overtone mode**			
	$f_{0,th}$ **(Hz)**	f_0 **(Hz)**	Q_0	$f_{1,th}$ **(Hz)**	f_1 **(Hz)**	Q_1
QTF#1	13746.59	14068.14	9140	86088.96	86612.38	18960
QTF#2	7577.81	7216.41	24520	47456.54	41028.76	20620
QTF#3	8419.79	8448.80	36150	52729.49	51008.62	30270
QTF#4	3479.25	3454.27	8850	21789.04	21503.81	32850
QTF#5	2913.42	2870.98	14990	18245.50	17747.47	49490
QTF#6	4244.88	4250.01	37710	26583.84	25413.00	75250

Theoretical values estimated using Eq. (15.11) are also listed and marked by the subscript "*th*," for both modes. Measured quality factor values are also reported for the fundamental (Q_0) and first overtone (Q_1) mode.

A good agreement between the experimental and theoretical frequency values was obtained, which confirms that it is possible to predict the resonance frequency of a QTF with good accuracy for both the fundamental and first overtone modes. The small discrepancies between experimental and theoretical values are due to the damping of the gas (which produces a shift of the resonance frequency, as predicted by the

Euler-Bernoulli model), additional weight of the electrode gold layers, dependence of the elasticity modulus of quartz on the crystallographic axes orientation, and deviations in geometry between the modeled and the actual QTFs. To study the dependence from different loss mechanisms, the quality factor values were measured as a function of the air pressure for both fundamental and first overtone modes. Apart from the main loss mechanisms described in the previous paragraph, any asymmetry between prong geometry results in an additional damping mechanism for the vibrating QTF prong. The influence of prongs' asymmetries on the overall QTF quality factor has been reported in several publications using classical mechanical models [101, 102]. For a standard 32.7 kHz QTF, a prong symmetry breaking caused by a mass difference within 0.3% produced a decrease of the Q-factor of <10% [102]. For this set of custom QTFs, such a fractional mass difference corresponds to a prong size variation of a few microns for the shortest dimension, assuming that the crystal width w is not affected by the QTFs fabrication process (since $T>w$). To experimentally evaluate the influence of the prongs size asymmetry on the overall quality factor, a statistical study by testing different QTF samples having the same geometry and belonging to different crystal benches, with the same experimental conditions were performed. All the QTF samples showed Q-factor values differing by less than 10%. This confirms that the QTFs fabrication process does not produce asymmetries in the geometry of the prongs that can affect the QTF Q-factor. The dependence of the measured quality factors on air pressure is reported in Fig. 15.13 for QTF#4.

For all QTFs, the pressure dependence of the Q-factor values follows the trend of Q_{air} reported in Fig. 15.9A, suggesting that the dominant loss mechanism is air damping for both modes. The air damping dependence on the prong size can also be investigated by comparing QTFs differing only in T or L. QTF#2 and QTF#4 share almost the same prong length (L=10 mm and L=11 mm for QTF#2 and QTF#4, respectively) and the crystal thickness (w=0.25 mm) but substantially differ in the prong thickness (T=0.9 and 0.5 mm for QTF#2 and QTF#4, respectively). According to Fig. 15.9B, a reduction of the prong width corresponds to an increase of the air damping mechanisms. At atmospheric pressure, the fundamental mode of QTF#2 exhibits a quality

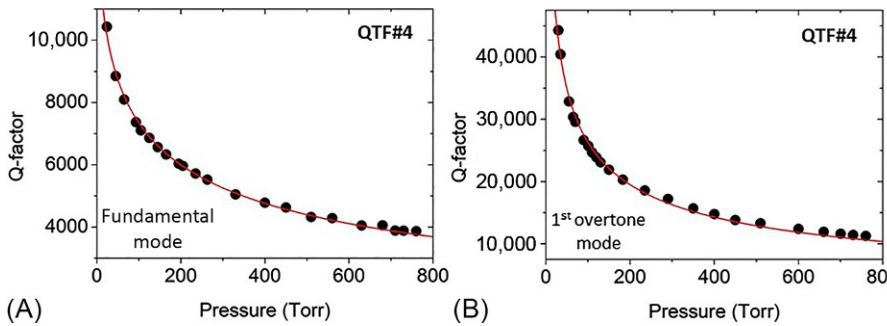

Fig. 15.13 Experimental quality factor values (●) as a function of the air pressure together with the best fit obtained by using Eq. (15.20) when QTF#4 oscillates at the fundamental (A) and the first overtone (B) mode.

factor (Q=8420), 2.2 higher than that measured for the QTF#4 (Q=3870). Similarly, a reduction of the prong length causes an increase of the air damping mechanisms, when other prong sizes are equal. This statement has been verified by comparing QTF#2 (L=10 mm, w=0.25, and T=0.9 mm) and QTF#5 (L=17 mm, w=0.25, and T=1.0 mm), having almost the same T but differing in L. At atmospheric pressure, the fundamental mode Q-factor of QTF#5 is ~5200, almost 1.6 times lower than that measured for the QTF#2. For the overtone modes, the air damping mechanisms are reduced (see Fig. 15.9A) and support losses start to dominate. Support losses strongly depend on the prong geometrical factor L/T (see Eq. 15.15). In the investigated set of QTFs, the highest L/T ratios are 22, 17.5, and 17 calculated for QTF#4, QTF#1, and QTF#5, respectively. At atmospheric pressure, for these QTFs the Q-factor for the first overtone mode are ~three times higher with respect to the Q-factor measured for the fundamental modes. Conversely, for QTF#2 and QTF#3, only a slight increase of Q-factor is observed (L/T=11.1 and 10.0 for QTF#2 and QTF#3, respectively). Eq. (15.20) was used to fit the experimental data reported in Fig. 15.13, for both the fundamental and overtone mode. The experimental data and the best fit obtained by using Eq. (15.20) for QTF#4 are reported in Fig. 15.13 for the fundamental and first overtone modes. From the fit, the pressure-independent quality factor contribution $Q(0)$ were extracted. Each contribution to $Q(0)$, Q_{TED} and Q_{sup}, can be related with the geometrical properties of the resonator: $Q_{sup} \propto L^3/T^3$ (Eq. 15.15), while $Q_{TED} \propto T^3/L^2$ (Eq. 15.16). Even if it is not possible to separate the two contributions of $Q(0)$, it was feasible to investigate the dependence of $Q(0)$ values from the geometrical parameters of the QTF prong, since Q_{sup} and Q_{TED} show opposite behaviors with the prong sizes. $Q(0)$ clearly showed a linear dependence on the T^3/L^2 ratios, provided that the relevant dissipation mechanism (after air damping) at the fundamental mode is related to the thermoelastic losses and support losses can be neglected [28]. This agrees with the results obtained in Ref. [26] in which the support losses were negligible for QTFs vibrating at the fundamental mode, since an empirical correlation between the quality factor and Tw/L parameter at a pressure as low as 50 torr was observed. Conversely, for the first overtone mode, $Q(0)$ values were positively correlated with L^3/T^3, indicating that the support losses contribution is not negligible for the overtone modes, even if a contribution due to thermoelastic damping is assumed to be present [28]. This result agrees with the theoretical model proposed by Hao (see Eq. 15.4) that predicts an increase of the support losses by a factor of B_0/B_1 ~12 when transitioning from the fundamental to the first overtone mode.

Custom QTFs with dual-tube mR

The first implementation of mR tubes with a custom-made QTF was reported in Ref. [103]. The QTF had the same design of QTF#2 with prong spacing of 0.8 mm, characterized by a fundamental resonance frequency of 7205 Hz and a quality factor of 8530 at atmospheric pressure. A pair of mR tubes having inner diameter of 1.3 mm was employed. The gap between the QTF and the tubes was fixed to 30 μm. Five different lengths ranging from 8.4 to 23 mm (half of the sound wavelength) were tested. Longer tubes were not tested due to the difficulty in laser beam alignment and focalization

between the QTF prongs. An erbium-doped fiber-amplified laser with an output power of 1500 mW was employed as the available excitation source for the QEPAS investigation. A CO_2 absorption feature located at 6325.14 cm^{-1} with a line intensity of 1.155×10^{-23} cm^{-1}/mol was selected as the optimum target line. These studies revealed that for a tube length of l=23 mm the SNR was improved by a factor of ~40 compared to that measured for the bare QTF. With this spectrophone configuration, the reported Q-factor decreased to ~6300, ~26% with respect to the bare QTF. The study in Ref. [103] lacks an investigation of different internal diameters. In addition, the influence of the spacing between the prongs and the QTF on the SNR was not studied. A more comprehensive study of the impact of the tubes geometry on the QEPAS sensor performance was described in Ref. [104] by employing QTF#6 operating in the first overtone mode. An investigation of the influence of the distance between the tubes and the QTF on both the SNR and the Q-factor was reported. The distance maximizing the SNR (~1090) is 140 µm and corresponds to a Q-factor of ~27,100. The Q-factor approaches asymptotically the bare QTF value (28,900) when the distance between the tubes and the QTF becomes larger than 500 µm and rapidly decreases when this distance is reduced, confirming that the shorter the QTF-tube distance, the higher the acoustical coupling between them. When the distance is shorter than 140 µm, the SNR decreases because of damping effects generated by the proximity of the tube end to the surface of the QTF. To study the influence of tubes internal diameter on QEPAS performance, three different IDs of 1.27 mm, 1.52 mm, and 1.75 mm were employed. For each ID a set of tubes with different length, varying from 4.8 to 7 mm was tested. The highest SNR (~1600, Q-factor ~25,000) was obtained using two tubes with an ID of 1.52 mm and a length of 5.3 mm. This optimal length falls between $\lambda_s/2$=6.76 mm and $\lambda_s/4$=3.38 mm. There was an optimal length maximizing the SNR for each ID: for the largest ID (1.75 mm) the optimal length is 5 mm, closer to $\lambda_s/4$ confirming that the prong spacing can be neglected and the two tubes are close to form a half-wave resonator. For an ID=1.27 mm the optimal length is 6 mm, which is closer to $\lambda_s/2$=6.76 mm. This behavior is similar to that observed for the standard 32.7 kHz QTF [29]. In Table 15.4, the optimum design parameters of a dual-tube spectrophone based on standard 32.7 kHz QTF, QTF#2 and QTF#4 have been listed.

Table 15.4 Best geometry parameters of dual-tube spectrophones realized for three different QTFs

	Prong spacing (mm)	**ID (mm)**	**$\lambda_s/2$ (mm)**	**L (mm)**	**QEPAS SNR enhancement**	**Ref.**
32 kHz QTF	0.3	0.60	5.25	4.4	30	[29]
QTF#2	0.8	1.30	23.89	23.0	40	[103]
QTF#6	1.0	1.52	6.76	5.3	15	[104]

Prong spacing, internal diameter of the tube (ID), sound half wavelength ($\lambda_s/2$), tube length (l), and enhancement of the QEPAS SNR with respect to bare QTF.

15.5 Novel QEPAS approaches exploiting custom QTFs

Starting in 2013, custom QTFs have been realized in QEPAS sensors following two guidelines: (i) reduction of the QTF fundamental frequency and (ii) increase in the prong spacing in order to facilitate the optical alignments and minimize the photothermal noise level. Larger prongs spacing led to the implementation of a single tube as acoustic mR system [105]. Custom QTFs designed to operate with fundamental flexural resonance mode frequency of a few kHz opened the way to the implementation of the first overtone flexural modes for QEPAS sensing [84, 85, 97, 98, 104]. Single-tube mR optimized for QTF overtone mode operation provided record QEPAS signal-to-noise gain factors of more than two orders of magnitude [106]. Furthermore, two innovative QEPAS approaches have been demonstrated: (i) double-antinode excited QEPAS (DAE-QEPAS), in which a laser beam excites simultaneously the two resonance antinode vibrational points of a QTF operating with the first overtone flexural mode [107], providing a record signal-to-noise amplification factor exploiting a dual acoustic mR system; and (ii) dual-gas QEPAS detection, where two laser sources excite the antinodes of both the fundamental and the first overtone flexural modes, enabling the simultaneous detection of two-gas species [108].

15.5.1 QEPAS with QTF vibrating at the first overtone flexural mode

Higher Q-factor values imply higher QEPAS signals [84]. Hence, when the first overtone mode of a QTF exhibits a quality factor higher than that of fundamental mode, a higher QEPAS signal is also expected. QTF#2, QTF#4, QTF#5 and QTF#6 have been employed in a QEPAS setup, operating both at the fundamental and first overtone mode [84, 104]. The first overtone mode of QTF#1 and QTF#3 cannot be used for QEPAS because f_1 exceeds 40 kHz (see Table 15.3). As discussed in previous sections, the focused laser spot must be located between the two prongs along the QTF axis and in one of antinodes points of the vibration profile (where the maximum vibration amplitude is allowed). The first overtone mode exhibits two antinode points; however, the second antinode point (close to the middle of the prong) is favorite with respect to the first antinode point located to the top of the prong, as discussed in Section 15.4.1. It was found that the QEPAS signal for QTF#5 was the largest when the laser beam was positioned at s_1=2 mm and s_2=9.5 mm from the top of the QTF#5 for the fundamental and first overtone mode, respectively. For QTF#2 it was found that s_1=1.2 mm and s_2=5.5 mm, for QTF#4 s_1=1.1 mm and s_2=6 mm, and for QTF#5, s_1=1.2 mm and s_2=12 mm [84, 104]. As discussed in Section 15.4.1, for the fundamental mode the optimum laser beam position is shifted toward the prong base with respect to the antinode point. This can be explained by considering that the closer to the prong top is the vertical position of the spherical-like acoustic source, the larger is the fraction of the pressure wave not hitting a prong. For the same reason, as mentioned before, when operating with an overtone mode, the second antinode is optimum with respect to the first antinode. The QEPAS signal depends on the gas sample pressure.

When the gas pressure decreases, the quality factor increases, while the sound propagation efficiency is lowered due to the decreased rate of gas molecular collisions. Thus, a tradeoff in pressure must be found in order to maximize the photoacoustic signal *S*. The QEPAS peak signal for the fundamental and first overtone modes were measured as a function of the gas pressure in the range 30–170 torr and exhibits a maximum value at 75 torr for all QTFs, varying by less than 5% in the 60–100 torr range, except for the first overtone mode of QTF#2 [84]. This different behavior is due to the substantially higher QTF#2 overtone mode frequency (41 kHz), with respect to the fundamental and overtone modes of the other two QTFs. Thus, a higher pressure is required to increase the energy relaxation time, so that the thermal waves in the gas can follow efficiently fast changes of the laser induced molecular vibration excitation. Indeed, for QTF#2 it was observed a maximum QEPAS signal for the overtone mode at 120 torr [84]. The influence of the modulation depth on the QEPAS signal was also investigated. All QTFs resonance modes exhibit their highest signal when using a modulation depth of 0.05 cm^{-1}, corresponding to a 5-mA modulation amplitude value. The QEPAS spectra show that the peak values measured for the first overtone mode are higher than those obtained using the fundamental mode for the QTF#4 (~2.2 times), QTF#5 (~5.3 times), and QTF#6 (~3.1 times), while the QEPAS signal acquired with overtone mode of the QTF#2 is ~7.1 times lower. These results clearly demonstrate that for QTF#4, QTF#5, and QTF#6 operating in the first overtone flexural mode is advantageous in terms of the optimum QEPAS signal [84]. As expected, this is a consequence of a higher quality factor for the overtone mode, with respect to the fundamental mode.

15.5.2 Single-tube mR systems

Due to the large prong spacing of custom QTFs, it was possible to position a single tube between the prongs of the QTF and thereby avoiding cutting the tube into two pieces, as shown in Fig. 15.14A.

In this case, the behavior of a single tube in the QEPAS spectrophone is that of an ideal one-dimensional acoustic resonator. The waist of the tube thickness was polished in order to reduce OD when it is larger than the prong spacing (see Fig. 15.14B). A pair of slits was opened on each side of the tube waist, symmetrically in the middle of the tube, where the acoustic pressure antinode is located. Sound waves exiting from two slits impacts on the internal surface of two prongs and excite in-plane antisymmetrical vibrational modes. This QEPAS configuration is named single-tube OB-QEPAS (SO-QEPAS). SO-QEPAS was reported for the first time in Ref. [105], employing the QTF#2 design. Three mR sets characterized by different internal diameters (0.55, 0.65, and 0.75 mm) and with different lengths, ranging from 47 mm (~λ_s) to 25 mm (~$\lambda_s/2$) have been tested. In all cases, the length of the slit is almost half of the outer diameter and its width is ~90 µm, since larger slits disperse the acoustic energy, while smaller sizes limit the acoustic energy escaping from the slits in the mR tubes. The maximum signal amplitude for ID=0.55 mm, 0.65 mm and 0.75 mm were obtained for tube 36, 39, and 38 mm long, respectively. These values

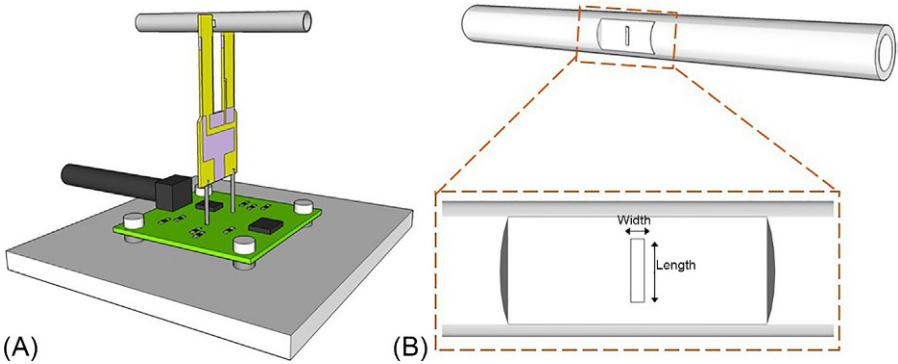

Fig. 15.14 (A) Sketch of a single-tube QEPAS spectrophone. (B) Three-dimensional view of the tube with an enlargement of the slit.

were larger than the half wavelength of the acoustic wave, indicating that the first harmonic acoustic standing waves in the resonator were partially distorted by the two resonator slits, causing a diverging flow from the tube toward the internal surface of the QTF. In contrast to the case of dual tube, the optimal tube length only slightly changes with the internal diameter, thus confirming that a single tube can be approximated by a 1D acoustic resonator. The SO-QEPAS configuration with an ID=0.65 mm and *l*=38 mm results in a maximum SNR, 128 times higher than of the bare QTF#2, with a quality factor of ~6700, ~20% lower than that of the bare QTF#2. The SO-QEPAS configuration was also employed with QTF#5 operating in the first overtone flexural mode at ~17.7 kHz [106]. The tube length was reduced due to the high overtone resonance frequency. This approach resulted in a more compact spectrophone, facilitating the laser beam alignment through the QTF and the mR tube. The tube has an internal diameter of 0.62 mm and the maximum SNR (~2300) was obtained for an optimal length of 14.5 mm, resulting ~50 times larger than that measured using the bare QTF operating in the first overtone resonance mode. The slit width and length were ~90 μm and ~200 μm, respectively. The SO-QEPAS configuration was also implemented for QTF#6 operating at its first overtone mode [104]. In order to find the optimum ID maximizing the SNR, a set of 4 tubes having length *l*=11 mm and different internal diameters was used. The highest SNR (~2060) was obtained with a tube having ID=0.88 m and l=11 mm. For these measurements, a slit width of ~100 μm, similar to that reported in Refs. [105, 106], was chosen. Since the prong width for QTF#6 is 800 μm, considerably wider than that of QTF#2 and QTF#5 (250 μm), slit widths larger than 100 μm were tested. With a slit width of 250 μm a SNR of ~3700, ~34 times larger than that measured using the bare QTF#6 operating in the first overtone resonance mode and a quality factor of ~26000, only 10% lower than that of the bare QTF#6, were obtained. The SNR decreased to ~2300 (Q=17700) when the slit width is enlarged up to 370 μm. The advantages of SO-QEPAS configuration with respect to dual-tube QEPAS are (i) a more compact QEPAS spectrophone (for QTF#2

the spectrophone length is reduced from 46 mm to 38 mm), providing easier optical alignment; (ii) a higher spectrophone *Q*-factor; (iii) a larger SNR (for QTF#2 the SNR measured with SO-QEPAS is 3.2 times higher than that measured with the best operating conditions for dual-tube QEPAS); and (iv) an optimal length of the tube not depending on the ID. As guidelines for future designs of SO-QEPAS configurations with novel designs of custom-made tuning forks, the main design parameters of the single tube with the geometrical parameters of the tuning fork were compared and listed in Table 15.5, for QTF#2, QTF#5 and QTF#6.

This range of values can be used as a starting point to design the optimal SO-QEPAS configuration when employing new QTF designs, thus avoiding extensive tube geometry investigations.

15.5.3 Double-antinode excited quartz-enhanced photoacoustic spectrophone

Differing from the fundamental flexural mode, the first overtone mode oscillation shows two antinodes, oscillating in counterphase. Hence, it is possible to excite two resonance antinode points simultaneously by using two laser beams if their phase shift is properly adjusted. The first demonstration of a DAE-QEPAS system was reported in Ref. [107], implementing QTF#5 and a dual-tube mR system. The schematic of the DAE-QEPAS spectrophone is depicted in Fig. 15.15A.

The QTF is positioned between the two mRs tubes to probe the acoustic vibration excited in the gas contained inside tubes and the two mRs are positioned at heights corresponding to the lower and higher QTF first overtone resonance antinode points.

A pigtailed DFB laser emitting at 1.37 µm was employed to generate the photoacoustic signal, by exciting a H_2O absorption line located at 7306.75 cm^{-1} with a line intensity of 1.8×10^{-20} cm/mol. The PZT phase compensator was used to adjust the phase between the two laser beams passing through the two mRs in order to maximize the QEPAS signal. The phase shift between the two antinode points was ~180 degree. The laser beam passed twice through the lower mR by means of a mirror and once through the upper mR, exciting the two QTF resonance antinodes simultaneously with a compensated phase. The largest QEPAS SNR was obtained employing 8.5-mm-long tubes for the two mRs. The achieved signal amplitude was ~3 times higher than that obtained with standard OB-QEPAS, ~100 times higher than that obtained with a bare QTF operating at the first overtone mode and ~500 times higher when operating at the fundamental flexural mode resonance. Further improvement of the SNR gain factor can be achieved either by assembling two single-tube mRs exploiting the SO-QEPAS configuration or by designing and implementing an octupole configuration for the QTF gold pattern in order to increase the charge collection efficiency of the first overtone flexural mode resonance (see Section 15.4.4). The possibility to increase the space between the prongs, potentially up to few millimeters will allow to employ mR tubes with a large ID, thereby simplifying optical alignment and making the QEPAS spectrophone less sensitive to external vibrations.

Table 15.5 Best geometry parameters of the single-tube spectrophone for three different QTFs.

	Resonance mode	**Prong spacing (mm)**	**ID (mm)**	Λ_s **(mm)**	***l*** **(mm)**	**Prong width (mm)**	**Slit width (mm)**	**QEPAS SNR enhancement**	**Ref.**
QTF#2	Fundamental	0.8	0.65	47.8	38.0	0.25	0.10	128	[105]
QTF#5	Overtone	0.7	0.62	19.3	14.5	0.25	0.10	50	[106]
QTF#6	Overtone	1.0	0.88	13.5	11.0	0.80	0.25	34	[104]

Prong spacing, internal diameter of the tube (ID), sound wavelength (λ_s), tube length (l), QTF prong width, slit width, and enhancement of the QEPAS SNR with respect to the case of bare QTF.

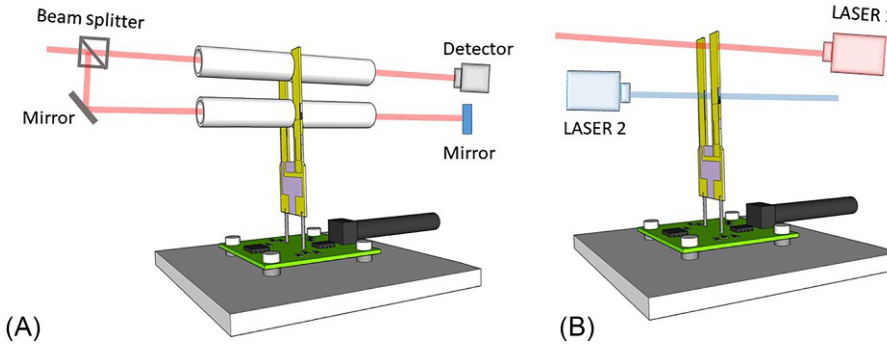

Fig. 15.15 (A) Schematic of the DAE-QEPAS spectrophone. The laser beam is splitted and sent through two dual-tube resonators located close to two antinode points of first overtone mode of the QTF. The laser beam passed twice through the lower tube by means of a mirror and once through the upper resonator tube, exciting the two QTF resonance antinodes simultaneously with a compensated phase. (B) Schematic of QEPAS spectrophone for dual-gas detection. One laser beam is focused close to the antinode point of the fundamental mode and a second beam to the second antinode point of the first overtone mode: in this way, both modes are excited simultaneously at two different frequencies.

15.5.4 Simultaneous dual-gas detection

Multi-gas online detection is a topic of considerable interest in recent years because of its important applications in environmental monitoring, medical diagnosis, industrial process control, agriculture and food industries and pollution monitoring. In several cases, like isotope concentration ratios, to retrieve the actual ratio value the concentration measurements of two isotopes must be performed simultaneously. This is also the case when the control and monitoring of relative concentration of two different gas target in a matrix that rapidly changes with time, as in agricultural applications or from sample to sample, as in breath analysis (e.g., NO and H_2O) is required. With a standard QEPAS approach, simultaneous gas detection is not feasible since the force sensing-based QTF cannot recognize the molecular source of a photo-induced acoustic wave. Even when a single laser source is able to separate two absorption features referred to two different gas species, there is a delay in time in the measurements of two different target gas concentrations, since the laser source has to be tuned from one absorption line to the other absorption line. However, due to the reduction in the fundamental resonance frequency achieved with custom QTFs, the first overtone flexural mode became available for QEPAS operation, allowing the simultaneous excitation of the QTF both on the fundamental and first overtone modes, using the same or two different laser sources. Recently, this approach was employed in the first demonstration of simultaneous dual-gas sensing, based on a QTF frequency division multiplexing technique [108]. The QTF in a dual-gas QEPAS sensor is excited simultaneously at the fundamental and first overtone flexural modes by two independently modulated lasers. The two target gases are detected via demodulation of the custom QTF piezoelectric signal at f_0 and f_1, by means of two lock-in amplifiers. The

schematic of a spectrophone for dual-gas QEPAS system is shown in Fig. 15.15B. In Ref. [108] QTF#5 was enclosed inside a gas cell and two laser beams were focused on the QTF plane. One laser beam was positioned near to the antinode point for the fundamental flexural mode and a second beam close to the first overtone flexural mode lower antinode point. A preliminary test with both laser sources tuned to the same wavelength at 1368.6 nm, resonant with a H_2O absorption line was performed to verify that there are no cross-talking effects between the fundamental and the first overtone flexural mode QEPAS signals, when the QTF was operated in the combined vibrations. No interference effects and no excess noise were observed when the QTF operates in combined vibrational motion with respect to the pure fundamental or first overtone flexural mode. The capability of the QEPAS sensor to perform simultaneous dual-gas spectral detection was demonstrated by implementing a DFB laser source targeting an acetylene (C_2H_2) absorption line located at 6541.96 cm^{-1} with a line strength of 3.5×10^{-20} $cm\cdot mol^{-1}$ [91] and a diode laser targeting a H_2O absorption line. The QEPAS spectra of both H_2O and C_2H_2 were acquired continuously without signal cross-talking. The sensor performance in terms of NNEA coefficient for H_2O and C_2H_2 are 9.12×10^{-7} and 1.51×10^{-7} $cm^{-1}\cdot W/\sqrt{Hz}$, respectively. The difference in performance is due to the different QEPAS response of QTF#5 for the fundamental vibrational mode with respect to the first overtone mode, which is five times higher for the latter. This difference can be adjusted by optimizing the QTF prong geometry, as largely discussed in Section 15.4.5.

Applications of a dual-gas QEPAS system include detection of gases with slow energy relaxation rates (such as NO, CO, and CH_4). As mentioned previously, to enhance the QEPAS signal, relaxation promoters (typically H_2O or SF_6) are added to the gas mixture and is crucial to control their concentration levels in a gas mixture. Thereby, the additional detection channel provided by the dual-gas QEPAS can be dedicated to monitor the relaxation promoter concentration and normalize the detected QEPAS signal. Further improvements of dual-gas QEPAS sensors performances can be achieved by adding dual- or single-tube acoustic mRs to enhance the generated photoacoustic wave intensity.

15.6 QEPAS trace gas detection results overview

MDLs can be quantified as the noise-equivalent concentration (NEC) or the minimum detectable absorption coefficient (α_{min}, in cm^{-1}), allowing different sensors to be compared without reference to the specific target gas. For estimates of noise and precision, the convention that NEC is the gas target concentration giving a signal equal to the root mean squared value of signal intensity variations (1σ) is usually employed. Although the QTF thermal noise represents the physical limit for sensor detection, QEPAS sensors typically do not to reach this ultimate noise level (~μVs). Therefore, for many sensor systems, white noise dominates, and SNR depends on the bandwidth Δf, being $SNR\propto\Delta f^{-1/2}$. Furthermore, it is important to also report the value of the measurement integration time τ used to obtain a certain noise limit. In Table 15.6, the

Table 15.6 Best QEPAS detections of trace gases.

Molecule	Wavelength (μm)	Laser source	Detection limit (ppb)	Ref.
O_3	0.28	LED	1270	[44]
O_2	0.76	DL	13000	[109]
C_2H_2	1.53	DL	85	[29]
HCN	1.53	DL	155	[83]
NH_3	1.53	DL	418	[110]
N_2H_4	1.53	DL	1000	[71]
H_2S	1.58	DL	734	[75]
HCl	1.74	DL	700	[111]
C_2H_6	3.34	ICL	7	[112]
C_3H_8	3.34	ICL	2000	[113]
H_2CO	3.53	ICL	550	[114]
CO_2	4.30	QCL	0.3	[79]
CO	4.60	QCL	1.5	[78]
C_2H_5OH	5.17	QCL	90	[115]
NO	5.26	QCL	5	[25]
SO_2	7.24	QCL	100	[116]
H_2O_2	7.73	QCL	75	[117]
CH_4	7.83	QCL	13	[118]
N_2O	7.83	QCL	6	[118]
C_2HF_5	8.26	QCL	13	[27]
C_2H_4	10.3	QCL	100	[119]
SF_6	10.5	QCL	0.05	[59]
CH_3OH	76.3	QCL	4000	[99]

The laser source, the wavelength, and MDLs are also listed in the table.

results obtained so far for QEPAS-based gas sensors are listed. For each gas target, it is reported the operating spectral region and the sensor performance in terms of NEC.

The signal integration time as well as the available optical power affects the NEC. For this reason, detection limits are reported in units of NNEA measured in $\mathrm{cm^{-1}} \cdot \mathrm{W} / \sqrt{\mathrm{Hz}}$, by normalizing the noise-equivalent absorption to a 1-Hz measurement bandwidth and to the laser optical power:

$$NNEA = \frac{\alpha_{\min} P}{\sqrt{\Delta f}} \tag{15.22}$$

NNEAs measured to date using QEPAS are better than the best conventional PAS results. A record NNEA of 3.75×10^{-11} $\mathrm{cm^{-1}} \cdot \mathrm{W} / \sqrt{\mathrm{Hz}}$ is obtained for CH_3OH detection at a gas pressure of 10 torr, employing a THz QCL coupled to custom bare QTF#5 [99]. This record value as been achieved also because THz spectral range is particularly suitable for the QEPAS technique, since rotational levels, typically involved in the gas relaxation processes, are up to three orders of magnitude faster with respect to mid-IR vibrational levels, thereby allowing allow low-pressure operation, providing high QTF resonance Q-factors, and consequentially large QEPAS signals [39, 99, 120].

The highest NNEA of 2.7×10^{-10} $cm^{-1}\cdot \le W/\sqrt{Hz}$ in the mid-IR spectral range was obtained for SF_6 detection at a gas pressure of 75 torr, employing an external cavity mid-IR QCL fiber coupled to the ADM with standard 32 kHz QTF acoustically coupled with dual-tube mR OB configuration. The sensitivity of the sensor is a result also of exceptionally large SF_6 absorption cross-sections and its fast V-T relaxation [32, 59]. The QEPAS detection sensitivity was usually been improved by adding a fast-relaxing promoter. For example, CO detection in N_2 achieved a low NNEA (5.3×10^{-7} $cm^{-1}\cdot W/\sqrt{Hz}$) confirming that the V-T relaxation of the CO fundamental vibration is slow for efficient acoustic generation at 32.7 KHz [121]. A propylene host was found to promote the V-T relaxation of CO leading to an improvement of the NNEA of one order of magnitude [122]. Similarly, N_2O is characterized by a slow V-T relaxation and in this case SF_6 was added to the gas sample to promote the V-T relaxation leading to a N_2O NEC of 7 ppb, for a 1-s lock-in integration time [121]. CO_2 is also a slow relaxing molecule and the presence of H_2O acted as a relaxation promoter. Indeed, increasing the water concentration up to 1.5% in gas mixtures containing CO_2 provided an enhancement of the QEPAS signal, leading to an MDL of 18 ppm for a 1-s lock-in integration time [22]. Higher H_2O concentrations resulted in a lower QEAPS signal, since the relaxation process of CO_2 molecules are dominated by CO_2–H_2O collisions. Similarly, Nitric Oxide is a slow relaxing molecule and the QEPAS-based NO detection was improved by a factor of almost 50 by the addition of 2% of H_2O with respect to dry NO in N_2 [24].

15.6.1 Long-term stability and Allan variance

While NNEA describes the sensor performance on a short time scale, measurements are required to characterize long-term drifts and establish the signal averaging limits. The approach, described in Ref. [123], introduces the Allan variance of time sequences of measurements to quantify the long-term stability of optical trace gas sensors. This analysis allows investigating drifts and establishing the sensor signal averaging limits. Given a set of M time-series data acquired with an integration time τ, its Allan variance $\sigma_y^2(\tau)$ is defined as:

$$\sigma^2{}_y(\tau) = \frac{1}{M}\sum_{k=1}^{M}\frac{1}{2}\left(y_{k+1}-y_k\right)^2 \tag{15.23}$$

where y_k is the kth data averaged over an integration time τ, $y_{k+1}-y_k$ is the difference between adjacent values of y_k, and M is the total number of data, usually of the order of 10^3–10^4. To estimate how $\sigma_y^2(\tau)$ changes with the integration time, Giglio et al. implemented a LabView-based code [124]. Starting from the set of M data acquired at an integration time τ_0 and assuming that there is no dead time between adjacent measurements, the software averages the values for y_1 and y_2 and obtains a new y_1 value averaged over $2\tau_0$. Subsequently, this routine averages values for y_3 and y_4 and changes them as a new value y_2 averaged over $2\tau_0$ and finally applies Eq. (15.23) to determine $\sigma_y^2(2\tau_0)$. The software repeats this process for other integer multiples m of τ_0 and at the end of the processing, it generates values for $\sigma_y^2(m\tau_0)$ as a function of $(m\tau_0)$. Thus, to perform an Allan variance σ_y^2 analysis, all the data subsets have to be stacked

together and treated as a single uninterrupted time sequence. Usually, the Allan deviation σ_y is shown instead of the variance and expressed in terms of absorption coefficient or absorbing gas concentration; thus, determining the minimum detectable concentration as a function of the integration time. As discussed in Section 15.2.1, a QTF can be modeled as an RLC circuit and its electrical response is measured by means of a transimpedance amplifier with a gain resistor R_g in the order of 10 MΩ. The root mean square of the QTF thermal (Johnson) noise is expressed by Eq. (15.7). R_g also introduces noise, which is several times lower than the thermal QTF noise and can be neglected for typical values of R in the range 10–100 kΩ, as in our case. Thermal noise determines the MDL of the QEPAS sensor. If the QTF thermal noise is the dominant noise source, the Allan deviation closely follows a $1/\sqrt{t}$ dependence, for the entire duration of the concentration measurements. It was verified that when a long-time acquisition of the QTF signal was performed in the absence of laser illumination (dark noise), the integration time trend matches the theoretically thermal one, thus confirming that for laser-OFF conditions only the Johnson noise influences the QEPAS sensor [124]. When the laser source is switched on, two different conditions must be discriminated, off- and on-resonance conditions, with the laser wavelength locked far from an absorption line absorption line or on its peak, respectively. The Allan deviation measured for the off-resonance condition follows the Johnson noise trend and is almost identical to the QEPAS dark noise, demonstrated for an integration time up to $\tau > 1000$ s, when a very good optical alignment and focusing conditions are reached. The Allan plot of the QTF signal for the on-resonance condition also follows the dark noise trend till a certain value where it reaches a minimum value. At longer integration times, the Allan plot increases. The MDL is usually referred to the turnover point of the Allan deviation plot; at longer τ values, the QEPAS sensitivity starts to deteriorate. Giglio et al. in Ref. [124] also demonstrated that, after the turnover point, laser power instabilities contribute with the photothermal induced noise to the increase in the QEPAS noise level, compromising the system stability and hence decreasing the MDL of the reported sensor system. Therefore, one has to reduce the laser power fluctuations to improve the sensor sensitivity. This requires the implementation of more stable laser current driver and temperature controller technologies as well as a reduction of mechanical vibrations. The turnover point, and the extent to which performance deteriorates thereafter, are both application- and installation-specific for a given sensor instrument.

15.6.2 Comparison with existing optical techniques

When comparing different techniques, a figure of merit that makes sense in one application is of limited value in another, or even difficult to calculate. A possible common metric to compare the performances of different types of laser-based sensors should take into account the available optical laser power, the strength of the selected absorption line and the integration time used in the measurements. In this case, the NNEA parameter, when it is possible to compute, represents the best choice. In Ref. [35], the performance of several gas detection techniques in terms of NNEA versus optical path length are compared. It should be noted that in most cases the reported NNEA was

obtained in a laboratory setting and such performances cannot easily be replicated in actual field environment. For example, it can be challenging to maintain the precise alignment needed in sensor systems with long equivalent optical path lengths. The techniques with the lowest *NNEA*, i.e., those capable to reach ppb and ppt gas detection concentrations, are those characterized by very long path lengths (up to tens of km), namely CDRS, ICOS and CEAS. However, PAS and in particular QEPAS shows very good performance, reaching NNEA in the 10^{-11} $cm^{-1} \cdot W / \sqrt{Hz}$ range, with the advantage of a much better sensor compactness [19, 98]. Three main approaches have to be followed to realize optical sensors with high sensitivity: (i) selection of optimal molecular transition in terms of absorption strength and absence of possible interfering gases; (ii) long optical path length and/or cavity optical build-up; (iii) efficient spectroscopic detection schemes. Since the QEPAS technique is characterized by direct proportionality between the signal amplitude and the laser power available for gas excitation, the higher the optical power focused between the QTF prongs, the lower will be the QEPAS sensor's MDL. Thus, the possibility to realize intracavity optical build-up and QEPAS detection sensor design may lead to

the realization of an optical sensor system with unprecedented detection sensitivity. Recently a

cavity-enhanced optical feedback-assisted PAS sensor was demonstrated for water vapor detection reaching a noise-equivalent absorption value of 1.9×10^{-10} $cm^{-1} \cdot W / \sqrt{Hz}$ [125]. Furthermore, the development of I-QEPAS allowed to increase the QEPAS sensor performance up to a factor of ~250, with an effective optical path length of 84 m [79, 80]. Since a bare QTF was used as an ADM, further improvements can be expected by adding a mR system to the ADM and detecting fast-relaxing gases (or employing custom QTFs with a resonance frequency <10 KHz), which can yield I-QEPAS sensitivities at ppq concentration levels and corresponding NNEA values down to 10^{-12} $cm^{-1} \cdot W / \sqrt{Hz}$.

15.6.3 Examples of real-world applications

15.6.3.1 Environmental monitoring

A quartz-enhanced photoacoustic sensor was employed to perform real-time and in situ atmospheric measurements of CH_4 and N_2O [118]. The QEPAS-based sensor system used a 7.83-μm CW, thermoelectrically cooled (TEC) DFB QCL, with an output power of 158 mW. The ADM was composed by a commercial 32.7 kHz QTF acoustically coupled with a dual-tube mR system, in OB configuration. The characteristic and performance of the QEPAS sensor prototype in the laboratory environment are reported in Ref. [126]. The targeted CH_4 and N_2O absorption lines were located at 1275.04 cm^{-1} and 1275.49 cm^{-1}, respectively, with absorption line strengths of 3.729×10^{-20} cm/mol and 1.407×10^{-19} cm/mol, respectively. MDLs of 13 ppb for CH_4 and 6 ppb for N2O, respectively, were reached. After the evaluation of its performance in laboratory environment, the developed QEPAS sensor was then installed in the Aerodyne Research, Inc. mobile laboratory (AML) in order to perform CH_4 and N_2O atmospheric concentration measurements. Considering the importance of CH_4

emissions from landfills and the potential of N_2O generation from waste disposal sites, the mixing ratios of these gas species around two urban solid waste disposal sites in the Greater Houston, Texas, area (WM Atascocita and BFI McCarty landfills) were monitored. A high-capacity cup mount was installed on the QEPAS sensor in order to isolate the system from vibrations induced by road bumps. Measurements were performed on three dates: September 7, 10, and 26, 2013. During in situ monitoring of CH_4 and N_2O, the QEPAS concentrations were compared with those measured by the AML van-based "QCL mini monitor" multipass optical sensor with a CH_4 detection sensitivity of 0.3 ppb and N_2O detection sensitivity of 0.060 ppb, in volume [118]. The two types of sensors yielded the same CH_4 and N_2O concentrations within <5% difference, thus verifying the precision and stability of the QEPAS sensor. On September 7, 2013, atmospheric CH_4 measurements at and around the WM Atascocita landfill were carried out. These measurements were performed from 12:00 to 16:28 p.m. central daylight time (CDT). The CH_4 mixing ratio remained stable at 1.8 ppm, until the AML approached the WM Atascocita, Texas, landfill at ~14:10 p.m., when a CH_4 plume of 10 ppm was detected. The highest CH_4 plumes (mixing ratios of 53, 14, and 25 ppm) were generated by waste trucks passing close to the AML. The second AML trip performed atmospheric CH_4 measurements at and around the BFI McCarty landfill, Texas, 77078 on September 10, 2013. These measurements were performed between ~8 a.m. and noon CDT. The average CH_4 mixing ratio detected near the BFI McCarty landfill was ~5 ppm based on averaging over measurements from 10:10 am until 11:40 a.m., while the highest mixing ratios observed, 16 and 27 ppm, were related to waste trucks passing near the AML. The third AML trip was based on monitoring atmospheric N_2O levels in the atmosphere around the BFI McCarty landfill on September 26, 2013. The measurements were performed between 10:15 am and 12:00 p.m. CDT. The N_2O level remained stable at its natural abundance near 323 ppb. However, when waste trucks passed close to the AML at two different times, 10:37 and 10:52 a.m., two spikes of N_2O were observed clearly, corresponding to 333 and 336 ppb, respectively. Furthermore, mixing ratios of approximately 350 ppb of N_2O were detected while the AML was circling the landfill from 11:22 to 11:32 a.m. Finally, enhancements of ~8 ppm of CH_4 and ~30 ppb of N_2O compared to their natural abundances were detected when the AML was next to the landfills or circling them at a distance of ~200 m. Due to dilution, mixing ratios decreased to background levels when the circling distance exceeded ~400 m.

15.6.3.2 Leak detection

Leak detection and localization are critical manufacturing quality control processes for several industrial fields such as mechatronics, biotechnology, petrochemical and automotive industries. There is a need for products and technologies that require hermetically closed areas, vessels, and tubes conveying pressurized gases or liquids, where leaks are a serious threat to products reliability and safety. Consequentially, considerable effort was invested during the last decades in developing gas leak detection systems with high sensitivity and stability to guarantee proper operation of a device in vacuum-sealed or high-pressure conditions. The selection of the leak sensing

method is mainly related to the required measurement precision. Differential pressure detectors are typically employed in industrial production chains, when the measurement time period allowed is a few seconds, and the precision for a single measurement is 1 Pa. These detectors monitor the pressure difference between two environments that are isolated from each other by forcing high-pressure gas into one of them. The disadvantage of this approach is the low sensitivity and the fluctuations of repeated measurements within ~4 Pa [127, 128]. Differential pressure test detection limits of 1×10^{-3} mbar·l/s can be realized. A different category of techniques is based on the detection of specific gas species (such as inert gases). An overpressure of a mixture containing the tracer gas is made inside the element under test and leaks are detected by tracing the target gas presence in the surrounding area. Halogen leak sensors require the pressurization of the system to be tested with an organic halide. The leak is found with a sniffer probe sensitive to traces of the halogen bearing gas. With such a system, leaks in the 10^{-7} mbar·l/s range can be identified [129]. Radioisotopes-based systems are able to detect leaks as small as 10^{-10} mbar·l/s. The item to be tested is placed in a chamber, which is filled with a radioactive tracer gas (typically krypton 85) [130]. If there is a leak, the radioactive gas diffuses through it inside the item. After removing the component from the test chamber, the radioactive gas flows outside through the leaks and can be detected by a radiation sensor. Mass spectroscopy leak sensors employ helium as the gas target [131, 132]. These systems have proven to be extremely sensitive, reaching a leak flow detection range of 10^{-11} mbar·l/s, which is suitable for quality control of critical components such as, for example, vehicle airbags or cardiac pacemaker cases. Hydrogen gas can also be used. The advantage of hydrogen is its very low natural background concentration in air (0.5 ppm). The main disadvantage is its flammability. In leak measurements, besides sensitivity and selectivity, the response time is important for the real-time detection of changes in gas tracer concentration. This suggested the use of QEPAS technique as leak sensors development. A QEPAS sensor designed for leak detection and using SF_6 as the leak tracer gas has been realized [133]. The QEPAS sensor employed a QCL as light source and an ADM composed by a standard 32.7 kHz QTF with a dual-tube OB mR system. The sensor targeted the SF_6 absorption line centered at 947.93 cm^{-1} with absorption strength of 1.4×10^{-20} cm/mol, which is well separated from the only feature potentially interfering in this range, a H_2O absorption band centered at 948.26 cm^{-1}. At the absorption peak, the available laser power was 25 mW. For an integration time of 1 sec, an MDL value of 3 ppb was achieved at the optimal gas mixture pressure of 75 torr. A leak test station was designed and realized, by implementing the QEPAS-based SF_6 sensor system, intended to detect and quantify leaks in mechatronics systems and components, such as vacuum valves and diesel injectors, which must operate at high pressures. The test station was validated by using a calibrated leak (ATEQ, model L1147AQ-N). Pure N_2 was passed through the test chamber at 0.67 mbar·l/s, while an overpressure of 1% SF_6:N_2 was applied to the certified leak. The mixture flows through the leak in the test chamber, due to the differential pressure (ΔP) between the test chamber and the SF_6:N_2 mixture. Thus, the gas sample coming out from the test chamber contains a SF_6 concentration that can be detected by the QEPAS-based SF_6 sensor system, operating in the locked mode, i.e., with the QCL frequency set to the center of the selected SF_6

absorption line. The ΔP was varied between 100 mbar and 1000 mbar for validation of the QEPAS leak test station. The resulting leak flow F_L was estimated by knowing the gas flows [133]. An excellent agreement was found with calibration data provided for the certified leak. Once validated, the leak test station was tested with real vacuum valve samples. The vacuum valves contained two separated chambers with internal and external connecting holes. A sealing piston, pushed by a pressure of 5 bars, closes the two internal holes and isolates the two chambers. Pure N_2 flows into valve chamber 1, while an overpressure of 1% SF_6:N_2 is created in chamber 2 via the related external holes. In the absence of any defect, the sealing piston was able to isolate the two chambers, avoiding contamination of the pure N_2 flow from SF_6 leak tracer gas. Valves with and without simulated defects were tested. For valve without defects only noise level leaks were measured by the QEPAS sensor, as expected. The leak detected for the smallest defect (with sizes of 20 µm) was 6.7×10^{-4} mbar·l/s [133]. However, the corresponding SF_6 trace gas concentration (10 ppm) was three orders of magnitude higher than the QEPAS sensor MDL value. Starting from a QEPAS sensor's NEC of 3 ppb at 1 s integration time and considering a N_2 gas carrier flow of 0.67 mbar·l/s, the minimum detectable leak was estimated in ~4.5×10^{-7} mbar·l/s, which can be decreased to ~4.5×10^{-9} mbar·l/s if pure SF_6 is used as leak test gas (instead of a 1% dilution in pure nitrogen). The obtained results showed that QEPAS-based SF_6 sensor system is competitive with state-of-the-art leak detection techniques, reaching sensitivity level obtainable only with radioisotope and mass spectroscopy systems, and with the advantages of lower cost, compact size and weight, faster response time and not requiring radioactive materials.

15.6.3.3 Hydrocarbon detection

For the petrochemical industry, the monitoring of hydrocarbons such as methane, ethane and propane represents one of the most efficient way to predict production outputs, estimate reserves, assess raw material quality of source rocks and reservoirs. For the analysis of downhole hydrocarbons mixture compositions, spectroscopic measurements are usually not performed on single gas component samples but on multicomponent mixtures. Hydrocarbons are characterized by the C–H bond. The fundamental bands of the vibrational levels due to C–H bond stretching lie in the 3–4 µm spectral window, while the energy of the bond bending varies in the range 7–8 µm [134, 135]. The exact values of transition energies and linewidths are determined by the boundary conditions related to the chemical structure of a specific hydrocarbon compound. The highest absorption cross sections for both methane and ethane correspond to the C–H stretching. The commercial availability of ICLs has led to new opportunities for trace detection of the main hydrocarbon gases [11, 12]. Indeed, the fundamental absorption bands of methane (CH_4), ethane (C_2H_6), propane (C_3H_8), ethylene (C_2H_4), propene (C_3H_6) and acetylene (C_2H_2) are located in the λ=3–4 µm spectral range. In Fig. 15.16, methane (C1) and ethane (C2) absorption cross sections are plotted in the range 2984–2992 cm^{-1} using data from the HITRAN database, at 50 torr [135].

At this pressure, the absorption line broadening due to collisions is low enough to allow distinguishing the fine structure of the absorption bands. Within a spectral range

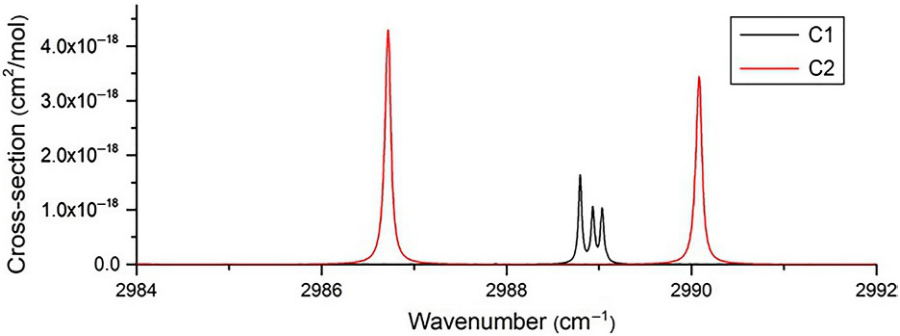

Fig. 15.16 Absorption cross sections at 50 torr pressure for methane (*black curve*) and ethane (*red curve*) in the range 2984–2992 cm^{-1} simulated using the HITRAN database [135].

of 3.5 cm^{-1}, there are two Lorentzian-like absorption lines of C2 and in the middle three partially merged lines of C1. The spectral separation between the C1 three-line structure and the two C2 lines guarantees a noninterfering detection of both species. A compact QEPAS sensor prototype for trace gas detection of methane, ethane and propane by using a single ICL source operating in the spectral range 3.342–3.349 μm has been realized and validated. For methane, the strongest response to photoacoustic excitation was achieved at a gas pressure of 200 torr. For ethane, the optimum gas mixture pressure was at 300 torr, providing a QEPAS signal only ~1.3 times higher with respect to the value recorded at the atmospheric pressure. This substantially differs from methane, where at atmospheric pressure the QEPAS signal decreased by ~70% with respect to the maximum signal recorded at 200 torr. This means that the C2 sensor works efficiently also at atmospheric pressure which is advantageous for in situ applications. For a 1-s integration time for online measurements, a detection limit of ~90 ppb for methane was achieved [113]. This is well below the sensitivity needed for a sensor aimed at hydrocarbon detection at a well site, where C1 concentrations are expected to be generally well above the ppm scale. A detection sensitivity of 7 ppb at 1 s of integration time was achieved for C2 and this represents a record for the QEPAS technique, opening the way to the implementation of QEPAS sensors for exploring and identifications of ethane reservoirs, an application of strong interest by petrochemical and plastic industries [113]. In addition, the QEPAS detection scheme is highly versatile, because in one single current scan C_1 and C_2 can be independently detected at sub-ppm scale and also dealt with unbalanced mixtures in which the methane concentration is two orders of magnitude or even higher in concentration with respect to ethane.

Relatively small molecules such as C1 or C2 present well-defined Lorentzian-like absorption features which can be detected by employing a WM detection scheme. However, mixtures, especially of larger molecules, often result in strongly overlapping and broadened spectra. In this case, a selective identification of distinct components and the determination of their concentrations are difficult due to wavelengths interference effects. In this context, propane (C3) is characterized by a broadband

spectrum in the 2–4 μm range. Since it is not listed in the HITRAN database, the PNNL database was taken as Ref. [136]. The C3 absorption cross sections are shown in Fig. 15.17.

Nevertheless, the lack of sharp Lorentzian-like features leads to a photoacoustic excitation intensity in a WM configuration that is low. In order to increase the propane QEPAS signal, all the measurements were carried out at atmospheric pressure, where multiple absorption lines merge to build a spectrum composed of well-separated bands. An MDL of 3 ppm was achieved for propane detection, at 1 s integration time [113]. The feasibility to perform photoacoustic C2/C3 gas detection (sharp Lorentzian-like C2 absorption feature within a C3 broadband spectrum) by fitting the QEPAS spectra was also demonstrated at atmospheric pressure [113]. Among different valid approaches such as multivariate analysis or machine learning, a fitting procedure based on a linear combination of reference spectra represented the most straightforward strategy.

15.6.3.4 Breath sensing

Breath analysis enables the diagnosis of a specific disease by analyzing the changes in breath gas composition. Tests revealing inflammatory processes in, for example, the lungs, neonatal jaundice and allergies based on inorganic gases concentrations are commercially available. Currently, there is also interest in volatile organic compound (VOC) measurement, as they can be used to diagnose multiple metabolic disorders. Today breath gas analysis is typically carried out using gas chromatography and mass spectrometers. Unfortunately cost and speed has limited its use mainly to research. The development of a cost-effective and portable platform opens the possibility of promoting breath gas analysis as a very promising in situ screening method. As an example of VOCs detection, measurements of ethylene (C_2H_4) traces from the human breath may provide insight into severity of oxidative stress and metabolic disturbances and may ensure optimal therapy and prevention of pathology at patients on continuous hemodialysis. Ethylene is a colorless, odorless, and flammable hydrocarbon.

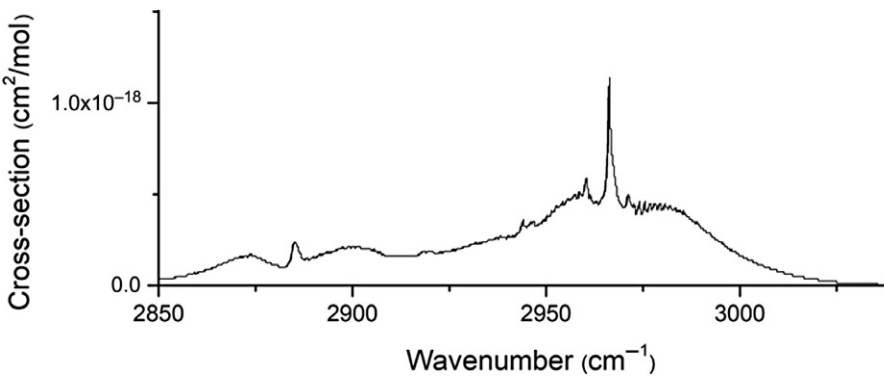

Fig. 15.17 Cross section of propane in the range 2850 to 3100 nm at atmospheric pressure, using PNNL database [136].

To detect ethylene, several methods and techniques have been proposed [137, 138]. It is primarily measured with stationary equipment in laboratories, such as gas chromatographic systems. Using a chromatographic column etched in silicon, a detection limit resolution of 3.8 ppb was reached [139]. However, such analytical technique does not offer real-time response, is costly, occupying a large spatial footprint, and not suitable for in situ and real-time measurements. The QEPAS technique for the detection and the quantification of ethylene have been exploited [119]. The C_2H_4 spectrum exhibits a well-resolved spectral structure with a high density of lines around 10.3 µm. They have no overlap with absorption lines of possible interferents present in standard air. According to the HITRAN database, the strongest C_2H_4 absorption line within the spectral tunability of the QCL is peaked at 966.38 cm^{-1} (10.347 µm), having a line strength of 2.21×10^{-20} cm/mol [140]. The QEPAS sensor architecture was kept as compact and robust as possible to allow applications requiring in human breath monitoring. A QCL emitting around 10.3 µm was used as light source to excite the ethylene molecules within a compact ADM, composed by a custom QTF#4 vibrating at the first overtone flexural mode resonance falling at 21.5 kHz and a dual-tube resonator system in OB configuration for sound amplification. The impact of the dual-tube resonator influences the QEPAS performance, as discussed in Section 15.2.2. The tubes lengths was set to $l=\lambda_s/4=4$ mm, mainly determined by the constrains of the ADM sizes. Using guidelines provided in Ref. [104], tubes having ID=0.84 mm and an outer diameter of 1.65 mm were selected. The gap between the tubes and the prong surfaces was fixed to ~50 µm. In this way, an enhancement factor of ~27 when a dual-tube resonator system is used with respect to the bare QTF was estimated. The optimal sensor operating conditions were found to occur at a gas pressure of 120 torr. The QEPAS sensor allowed for rapid measurements (100 ms integration time) down to a detection limit of 100 ppb of C_2H_4 detection in N_2. The MDL was improved to ~30 ppb by setting the integration time at 10 sec, corresponding to a minimum absorption coefficient $\alpha_{min}=6.02\times10^{-8}$ cm^{-1}. In this last case, considering an optical power of 61.6 mW and a lock-in detection bandwidth of 1.6675 Hz, a NNEA of 2.87×10^{-9} $cm^{-1}\cdot W/\sqrt{Hz}$ was calculated [104].

The development of compact optical sensors for nitric oxide (NO) detection is also of interest for medical diagnostics. Nitric oxide is involved in many vital physiological processes in the human body and elevated levels of NO in exhaled human breath is correlated with airway inflammation in asthmatic patients. Hence, NO can be used as a biomarker of asthma and inflammatory lung diseases such as chronic obstructive pulmonary disease. According to the HITRAN database [140] the fundamental absorption band of NO is located in the spectral region from 1780 to 1950 cm^{-1}. A QEPAS-based NO sensor, utilizing a CW, thermoelectrically cooled EC-QCL emitting at 5.26 µm as a light source and an ADM composed by a standard 32.7-kHz QTF coupled with a pair of mR tubes in OB configuration has been realized and validated [24, 25]. The EC-QCL allowed for access to the strong and quasi-interference-free absorption doublet $R(6.5)$ at 1900.075 cm^{-1}, which is unresolved at the optimal working pressure of 250 torr. NO detection for exhaled breath analysis, automotive exhaust assumes a presence of water vapor in the gas sample. Therefore, a study of the H_2O influence on the NO sensor performance was performed. The V-T energy transfer time for

NO is dependent on the presence of other molecules and intermolecular interactions. Due to the high energy of the first vibrational state of NO, the V-T energy transfer is slow, for example, in dry N_2 the relaxation time is τ_{VT}=0.3 ms and so $\omega\tau_{VT} \gg 1$ (see Eq. 15.4). The addition of H_2O vapor enhances the V-T energy transfer rate. Therefore, the presence of water in the NO/N_2 gas mixture results in an increase of the detected NO QEPAS signal amplitude. Once the $\omega\tau_{VT}<1$ condition is satisfied, the amplitude of the photoacoustic signal is not affected by τ_{VT} variations. Therefore, an increase of H_2O concentration beyond a certain level has a negligible effect on the PAS signal. QEPAS experiments should be performed at such signal saturation conditions. For a 2.5% water vapor concentration, a 130 times enhancement factor was achieved with respect to the case of no water in the NO/N_2 gas mixture [24]. Due to instrumental limitations of the humidifier, a condition of 5% water vapor concentration, which is similar to the concentration in exhaled human breath, was not experimentally determined. However, by using a fitting procedure, an enhancement factor of 146 times in the case of a 5% water vapor concentration was estimated. For QEPAS sensor validation, a constant water concentration of 2.5% was added to the NO/N_2 mixture using a Nafion material-based humidifier (PermaPure). The MDL estimated with a 1-s averaging time was 4.9 ppb, corresponding to a NNEA of 5.6×10^{-9} $\mathrm{cm^{-1}\cdot W/\sqrt{Hz}}$ (66 mW optical excitation power) [24, 25]. However, different water vapor concentrations lead to different sensitivities. Hence it is necessary to control and monitor the water concentration that is present in a NO QEPAS-based sensor. This issue can be avoided by using custom QTFs with a lower resonance frequency.

15.7 Conclusions and future developments

This chapter has focused on recent advances in the QEPAS sensing technique for the detection and monitoring of trace gas species. Progress to date in terms of custom QTF development, ADM configurations and new approaches for QEPAS sensing have been presented. Compared with a 32-kHz QTF coupled with a dual-tube mR system (which represents the standard approach for QEPAS sensors) the development of custom tuning forks resulted in better QEPAS sensing performance, providing an improvement up to four times for SNR and a 1.5 times for NNEA (1.21×10^{-8} $\mathrm{cm^{-1}\cdot W/\sqrt{Hz}}$ for QTF#5 as compared to 1.8×10^{-8} $\mathrm{cm^{-1}\cdot W/\sqrt{Hz}}$ for the 32 kHz QTF). Furthermore, the possibility to increase the prong spacing makes the optical alignment less critical, especially with laser sources having poor spatial beam quality. Custom QTFs allowed the extension of the QEPAS technique in the THz range, where, due to the fast rotational-vibrational relaxation rates, the QEPAS technique is more efficient, as demonstrated by the record NNEA factor achieved so far (3.75×10^{-11} $\mathrm{cm^{-1}\cdot W/\sqrt{Hz}}$). The reduction of the fundamental flexural mode resonance in custom QTFs opened the way to the exploitation of the first overtone mode for QEPAS sensing. This leads to demonstration of new approaches such as the double-antinode excited QEPAS and simultaneous dual-gas detection, the latter thanks to the possibility to excite the QTF at the fundamental and the first overtone flexural modes, simultaneously.

In conclusion, several novel approaches of QEPAS-based trace gas sensors have been demonstrated, potentially improving the sensitivity, size and robustness with detection sensitivities comparable to others bulky optical detection techniques, making QEPAS mature for real-world applications, including environmental monitoring, industrial processes control, and biomedical applications. The compactness and robustness make possible the extension of the QEPAS technique to other real-world sensing applications, such as gas sensing on drones and on rail vehicles.

References

[1] I. Galli, S. Bartalini, S. Borri, P. Cancio, D. Mazzotti, P. de Natale, G. Giusfredi, Molecular gas sensing below parts per trillion: radiocarbon-dioxide optical detection, Phys. Rev. Lett. 107 (2011) 270802: 1–270802:4.

[2] T. Tomberg, M. Vainio, T. Hieta, L. Halonen, Sub-parts-per-trillion level sensitivity in trace gas detection by cantilever-enhanced photo-acoustic spectroscopy, Sci. Rep. 8 (2018) 1848. 1-1848:7.

[3] G. Berden, R. Engeln (Eds.), Cavity Ring-Down Spectroscopy Techniques and Applications, first ed., John Wiley & Sons Ltd, Chichester, West Sussex, UK, 2009.

[4] G. Gagliardi, H.P. Loock, Cavity-Enhanced Spectroscopy and Sensing, Springer, London, 2014.

[5] M.R. McCurdy, Y.A. Bakhirkin, F.K. Tittel, Quantum cascade laser-based integrated cavity output spectroscopy of exhaled nitric oxide, Appl. Phys. B Lasers Opt. 85 (2006) 445–452.

[6] A. Elia, P.M. Lugarà, C. di Franco, V. Spagnolo, Photoacoustic techniques for trace gas sensing based on semiconductor laser sources, Sensors 9 (2009) 9616–9628.

[7] M.L. Viegerov, Eine Methode der Gasanalyse, Beruhend auf der Optisch-Akustischen Tyndall-Rontgeners- ¨cheinung, Dokl. Akad. Nauk SSSR 19 (1938) 687–688.

[8] K.F. Luft, Über eine neue methode der registrierenden gasanalyse mit hilfe der absorption ultraroter strahlen ohne spectrale zerlegung, Z. Tech. Phys. 5 (1943) 97–104.

[9] E.L. Kerr, J.G. Atwood, The laser illuminated absorptivity spectrophone: a method for measurement of weak absorptivity in gases at laser wavelengths, Appl. Opt. 7 (1968) 915–921.

[10] L.B. Kreuzer, N.P. Kenyon, C.K.N. Patel, Air pollution: sensitive detection of ten pollutant gases by carbon monoxide and carbon dioxide lasers, Science 177 (1972) 347–349.

[11] E. Max, L.-G. Rosengren, Characteristics of a resonant opto-acoustic gas concentration detector, Opt. Commun. 11 (1974) 422–426.

[12] G. Busse, B. Bullemer, Use of the opto-acoustic effect for rapid scan Fourier Spectroscopy, Infrared Phys. 18 (1978) 255–256.

[13] J. Fonsen, V. Koskinen, K. Roth, J. Kauppinen, Dual cantilever enhanced photoacoustic detector with pulsed broadband IR-source, Vib. Spectrosc. 50 (2009) 214–217.

[14] M.E. Webber, M. Pushkarsky, C.K.N. Patel, Fiber-amplifier-enhanced photoacoustic spectroscopy with near-infrared tunable diode lasers, Appl. Opt. 42 (2003) 2119–2126.

[15] F.G.C. Bijnen, F.J.M. Harren, J. Reuss, Geometrical optimization of a longitudinal resonant photoacoustic cell for sensitive and fast trace gas detection, Rev. Sci. Instrum. 67 (1996) 2914–2923.

[16] A. Berrou, M. Raybaut, A. Godard, M. Lefebvre, High-resolution photoacoustic and direct absorption spectroscopy of main greenhouse gases by use of a pulsed entangled cavity doubly resonant OPO, Appl. Phys. B 98 (2010) 217–230.

[17] C. Fischer, R. Bartlome, S.W. Sigrist, The potential of mid-infrared photoacoustic spectroscopy for the detection of various doping agents used by athletes, J. Appl. Phys. B 85 (2006) 289–294.
[18] A.A. Kosterev, Y.A. Bakhirkin, R.F. Curl, F.K. Tittel, Quartz-enhanced photoacoustic spectroscopy, Opt. Lett. 27 (2002) 1902–1904.
[19] P. Patimisco, G. Scamarcio, F.K. Tittel, V. Spagnolo, Quartz-enhanced photoacoustic spectroscopy: a review, Sensors 14 (2014) 6165–6206.
[20] W.H. Flygare, Triplet state. Its radiative and nonradiative properties, Acc. Chem. Res. 1 (1968) 121–127.
[21] A.A. Kosterev, F.K. Tittel, D. Serebryakov, A.L. Malinovsky, I. Morozov, Applications of quartz tuning forks in spectroscopic gas sensing, Rev. Sci. Instrum. 76 (2005) 1–9.
[22] G. Wysocki, A.A. Kosterev, F.K. Tittel, Influence of molecular relaxation dynamics on quartz-enhanced photoacoustic detection of CO2 at λ=2 μm, Appl. Phys. B Lasers Opt. 85 (2006) 301–306.
[23] A.A. Kosterev, Y.A. Bakhirkin, F.K. Tittel, S. McWhorter, B. Ashcraft, QEPAS methane sensor performance for humidified gases, Appl. Phys. B 92 (2008) 103–109.
[24] V. Spagnolo, A.A. Kosterev, L. Dong, R. Lewicki, F.K. Tittel, NO trace gas sensor based on quartz-enhanced photoacoustic spectroscopy and external cavity quantum cascade laser, Appl. Phys. B Lasers Opt. 100 (2010) 125–130.
[25] L. Dong, V. Spagnolo, R. Lewicki, F.K. Tittel, Ppb-level detection of nitric oxide using an external cavity quantum cascade laser based QEPAS sensor, Opt. Express 19 (2011) 24037–24045.
[26] P. Patimisco, A. Sampaolo, L. Dong, M. Giglio, G. Scamarcio, F.K. Tittel, V. Spagnolo, Analysis of the electro-elastic properties of custom quartz tuning forks for optoacoustic gas sensing, Sensors Actuators B Chem. 227 (2016) 539–546.
[27] A.A. Kosterev, P.R. Buerki, L. Dong, M. Reed, T. Day, F.K. Tittel, QEPAS detector for rapid spectral measurements, Appl. Phys. B 100 (2010) 173–180.
[28] P. Patimisco, A. Sampaolo, V. Mackowiak, H. Rossmadl, A. Cable, F.K. Tittel, V. Spagnolo, Loss mechanisms determining the quality factors in quartz tuning forks vibrating at the fundamental and first overtone modes. IEEE Trans. Ultrason. Ferroelectr. Freq. Control (2018), https://doi.org/10.1109/TUFFC.2018.2853404.
[29] L. Dong, A.A. Kosterev, D. Thomazy, F.K. Tittel, QEPAS spectrophones: design, optimization, and performance, Appl. Phys. B Lasers Opt. 100 (2010) 627–635.
[30] K. Liu, X. Guo, H. Yi, W. Chen, W. Zhang, X. Gao, Off-beam quartz-enhanced photoacoustic spectroscopy, Opt. Lett. 34 (2009) 1594–1596.
[31] K. Liu, H. Yi, A.A. Kosterev, W. Chen, L. Dong, L. Wang, T. Tan, W. Zhang, F.K. Tittel, X. Gao, Trace gas detection based on off-beam quartz enhanced photoacoustic spectroscopy: optimization and performance evaluation, Rev. Sci. Instrum. 81 (2010) 103103: 1–103103:6.
[32] V. Spagnolo, P. Patimisco, S. Borri, G. Scamarcio, B.E. Bernacki, J. Kriesel, Mid-infrared fiber-coupled QCL-QEPAS sensor, Appl. Phys. B Lasers Opt. 112 (2013) 25–33.
[33] N. Petra, J. Zweck, A.A. Kosterev, S.E. Minkoff, D. Thomazy, Theoretical analysis of a quartz-enhanced photoacoustic spectroscopy sensor, Appl. Phys. B Lasers Opt. 94 (2009) 673–680.
[34] D.V. Serebryakov, I.V. Morozov, A.A. Kosterev, V.S. Letokhov, Laser microphotoacoustic sensor of ammonia traces in the atmosphere, IEEE J. Quantum Electron. 40 (2010) 167–172.
[35] J. Hodgkinson, R.P. Tatam, Optical gas sensing: a review, Meas. Sci. Technol. 24 (2013) 012004: 1-012004:59.

[36] B.W.M. Moeskops, S.M. Cristescu, F.J.M. Harren, Sub-part-per-billion monitoring of nitric oxide by use of wavelength modulation spectroscopy in combination with a thermoelectrically cooled, continuous-wave quantum cascade laser, Opt. Lett. 31 (2006) 823–825.

[37] D.S. Bomse, A.C. Stanton, J.A. Silver, Frequency modulation and wavelength modulation spectroscopies: comparison of experimental methods using a lead-salt diode laser, Appl. Opt. 31 (1992) 718–731.

[38] P. Patimisco, A. Sampaolo, Y. Bidaux, A. Bismuto, M. Scott, J. Jiang, A. Muller, J. Faist, F.K. Tittel, V. Spagnolo, Purely wavelength- and amplitude-modulated quartz-enhanced photoacoustic spectroscopy, Opt. Express 24 (2016) 25943–25954.

[39] P. Patimisco, S. Borri, A. Sampaolo, H.E. Beere, D.A. Ritchie, M.S. Vitiello, G. Scamarcio, V. Spagnolo, A quartz enhanced photo-acoustic gas sensor based on a custom tuning fork and a terahertz quantum cascade laser, Analyst 139 (2014) 2079–2087.

[40] Y. Bidaux, A. Bismuto, P. Patimisco, A. Sampaolo, T. Gresch, G. Strubi, S. Blaser, F.K. Tittel, V. Spagnolo, A. Muller, J. Faist, Mid infrared quantum cascade laser operating in pure amplitude modulation for background-free trace gas spectroscopy, Opt. Express 24 (2016) 26464–26471.

[41] R. Lewicki, G. Wysocki, A.A. Kosterev, F.K. Tittel, QEPAS based detection of broadband absorbing molecules using a widely tunable, cw quantum cascade laser at 8.4 μm, Opt. Express 15 (2007) 7357–7366.

[42] M.D. Wojcik, M.C. Phillips, B.D. Cannon, M.S. Taubman, Gas-phase photoacoustic sensor at 8.41 μm using quartz tuning forks and amplitude-modulated quantum cascade lasers, Appl. Phys. B Lasers Opt. 85 (2006) 307–313.

[43] H. Yi, K. Liu, S. Sun, W. Zhang, X. Gao, Theoretical analysis of off beam quartz-enhanced photoacoustic spectroscopy sensor, Opt. Commun. 285 (2012) 5306–5312.

[44] S. Bottger, M. Koehring, U. Willer, W. Schade, Off-beam quartz-enhanced photoacoustic spectroscopy with LEDs, Appl. Phys. B Lasers Opt. 113 (2013) 227–232.

[45] T. Rück, R. Bierl, F.-M. Matysik, NO_2 trace gas monitoring in air using off-beam quartz enhanced photoacoustic spectroscopy (QEPAS) and interference studies towards CO_2, H_2O and acoustic noise, Sensors Actuators B Chem. 255 (2018) 2462–2471.

[46] M. Helman, H. Moser, A. Dudkowiak, B. Lendl, Off-beam quartz-enhanced photoacoustic spectroscopy-based sensor for hydrogen sulfide trace gas detection using a mode-hop-free external cavity quantum cascade laser, Appl. Phys. B Lasers Opt. 123 (2017) 141. 1-141:8.

[47] S. Schilt, A.A. Kosterev, F.K. Tittel, Performance evaluation of a near infrared QEPAS based ethylene sensor, Appl. Phys. B Lasers Opt. 95 (2009) 813–824.

[48] Y. Ma, Y. Tong, Y. He, X. Yu, F.K. Tittel, High-power DFB diode laser-based CO-QEPAS sensor: optimization and performance, Sensors 18 (2018) 122. 1-122:8.

[49] Z. Wang, Q. Wang, J.Y.-L. Ching, J.C.-Y. Wu, G. Zhang, W. Ren, A portable low-power QEPAS-based CO_2 isotope sensor using a fiber-coupled interband cascade laser, Sensors Actuators B Chem. 246 (2017) 710–715.

[50] C. Shi, D. Wang, Z. Wang, L. Ma, Q. Wang, K. Xu, S.-C. Chen, W. Ren, A mid-infrared fiber-coupled QEPAS nitric oxide sensor for real-time engine exhaust monitoring, IEEE Sensors J. 17 (2017) 7418–7424.

[51] J.A. Harrington, A review of IR transmitting, hollow waveguides, Fiber Int. Opt. 19 (2000) 211–217.

[52] C.M. Bledt, J.A. Harrington, J.M. Kriesel, Loss and modal properties of Ag/AgI hollow glass waveguides, Appl. Opt. 51 (2012) 3114–3119.

[53] R. Nubling, J.A. Harrington, Launch conditions and mode coupling in hollow glass waveguides, Opt. Eng. 37 (1998) 2454–2458.
[54] P. Patimisco, V. Spagnolo, M.S. Vitiello, G. Scamarcio, C.M. Bledt, J.A. Harrington, Low-loss hollow waveguide fibers for mid-infrared quantum cascade laser sensing applications, Sensors 13 (2013) 1329–1340.
[55] P. Patimisco, A. Sampaolo, L. Mihai, M. Giglio, J. Kriesel, D. Sporea, G. Scamarcio, F.K. Tittel, V. Spagnolo, Low-loss coupling of quantum cascade lasers into hollow-core waveguides with single-mode output in the 3.7–7.6 μm spectral range, Sensors 16 (2016) 533. 1-533:11.
[56] P. Patimisco, A. Sampaolo, M. Giglio, J.M. Kriesel, F.K. Tittel, V. Spagnolo, Hollow core waveguide as mid-infrared laser modal beam filter, J. Appl. Phys. 118 (2015) 113102.
[57] A. Sampaolo, P. Patimisco, J.M. Kriesel, F.K. Tittel, G. Scamarcio, V. Spagnolo, Single mode operation with mid-IR hollow fibers in the range 5.1-10.5 μm, Opt. Express 23 (2015) 195–204.
[58] M. Giglio, P. Patimisco, A. Sampaolo, J.M. Kriesel, F.K. Tittel, V. Spagnolo, Low-loss and single-mode tapered hollow-core waveguides optically coupled with interband and quantum cascade lasers, Opt. Eng. 57 (2017) 011004.
[59] V. Spagnolo, P. Patimisco, S. Borri, G. Scamarcio, B.E. Bernacki, J. Kriesel, Part-per-trillion level SF6 detection using a quartz enhanced photoacoustic spectroscopy-based sensor with single-mode fiber-coupled quantum cascade laser excitation, Opt. Lett. 37 (2012) 4461–4463.
[60] M. Siciliani de Cumis, S. Viciani, S. Borri, P. Patimisco, A. Sampaolo, G. Scamarcio, P. De Natale, F. D'Amato, V. Spagnolo, Widely-tunable mid-infrared fiber-coupled quartz-enhanced photoacoustic sensor for environmental monitoring, Opt. Express 22 (2014) 28222–28231.
[61] S. Viciani, M. Siciliani de Cumis, S. Borri, P. Patimisco, A. Sampaolo, G. Scamarcio, P. De Natale, F. D'Amato, V. Spagnolo, A quartz-enhanced photoacoustic sensor for H2S trace-gas detection at 2.6 μm, Appl. Phys. B Lasers Opt. 119 (2015) 21–27.
[62] Y. Cao, W. Jin, L.H. Ho, Gas detection with evanescent-wave quartz-enhanced photoacoustic spectroscopy, Proc. SPIE 8351 (2012). 835121: 1–835121:6.
[63] Y. Cao, W. Jin, L.H. Ho, Z. Liu, Evanescent-wave photoacoustic spectroscopy with optical micro/nano fibers, Opt. Lett. 37 (2012) 214–216.
[64] Z. Li, Z. Wang, Y. Qi, W. Jin, W. Ren, Improved evanescent-wave quartz-enhanced photoacoustic CO sensor using an optical fiber taper, Sensors Actuators B Chem. 248 (2017) 1023–1028.
[65] H. Wu, L. Dong, W. Ren, W. Yin, W. Ma, L. Zhang, S. Jia, F.K. Tittel, Position effects of acoustic micro-resonator in quartz enhanced photoacoustic spectroscopy, Sensors Actuators B Chem. 206 (2015) 364–370.
[66] L. Dong, H. Wu, H. Zheng, Y. Liu, X. Liu, W. Jiang, L. Zhang, W. Ma, W. Ren, W. Yin, S. Jia, F.K. Tittel, Double acoustic microresonator quartz-enhanced photoacoustic spectroscopy, Opt. Lett. 39 (2014) 2479–2482.
[67] Y. Ma, X. Yu, G. Yu, X. Li, J. Zhang, D. Chen, R. Sun, F.K. Tittel, Multi-quartz enhanced photoacoustic spectroscopy, Appl. Phys. Lett. 107 (2015) 021106.
[68] H. Zheng, X. Yin, L. Dong, H. Wu, X. Liu, W. Ma, L. Zhang, W. Yin, S. Jia, Multi-quartz enhanced photoacoustic spectroscopy with different acoustic microresonator configurations, J. Spectrosc. 2015 (2015). 218413: 1-218413:6.
[69] Y. Liu, J. Chang, J. Lian, Z. Liu, Q. Wang, Z. Qin, Quartz-enhanced photoacoustic spectroscopy with right-angle prism, Sensors 16 (2016) 214. 1-214:7.

[70] V. Spagnolo, L. Dong, A.A. Kosterev, D. Thomazy, J. Doty, F.K. Tittel, Modulation cancellation method for measurements of small temperature differences in a gas, Opt. Lett. 36 (2011) 460–462.
[71] V. Spagnolo, L. Dong, A.A. Kosterev, D. Thomazy, J. Doty, F.K. Tittel, Modulation cancellation method in laser spectroscopy, Appl. Phys. B Lasers Opt. 103 (2011) 735–742.
[72] V. Spagnolo, L. Dong, A.A. Kosterev, F.K. Tittel, Modulation cancellation method for isotope $^{18}O/^{16}O$, Opt. Express 20 (2012) 3401–3407.
[73] H. Zheng, L. Dong, X. Yin, X. Liu, H. Wu, L. Zhang, W. Ma, W. Yin, S. Jia, Ppb-level QEPAS NO_2 sensor by use of electrical modulation cancellation method with a high power blue LED, Sensors Actuators B Chem. 208 (2015) 173–179.
[74] H. Wu, L. Dong, X. Liu, H. Zheng, X. Yin, W. Ma, L. Zhang, W. Yin, S. Jia, Fiber-amplifier-enhanced QEPAS sensor for simultaneous trace gas detection of NH_3 and H_2S, Sensors 15 (2015) 26743–26755.
[75] H. Wu, L. Dong, H. Zheng, X. Liu, X. Yin, W. Ma, L. Zhang, W. Yin, S. Jia, F.K. Tittel, Enhanced near-infrared QEPAS sensor for sub-ppm level H_2S detection by means of a fiber amplified 1582 nm DFB laser, Sensors Actuators B Chem. 221 (2015) 666–672.
[76] L. Dong, R. Lewicki, K. Liu, P.R. Buerki, M.J. Weida, F.K. Tittel, Ultra- sensitive carbon monoxide detection by using EC-QCL based quartz-enhanced photoacoustic spectroscopy, Appl. Phys. B Lasers Opt. 107 (2012) 275–283.
[77] H. Wu, L. Dong, H. Zheng, Y. Yu, W. Ma, L. Zhang, W. Yin, L. Xiao, S. Jia, F.K. Tittel, Beat frequency quartz-enhanced photoacoustic spectroscopy for fast and calibration-free continuous trace-gas monitoring, Nat. Commun. 8 (2017) 15331.
[78] Y. Ma, R. Lewicki, M. Razeghi, F.K. Tittel, QEPAS based ppb-level detection of CO and N_2O using a high power CW DFB-QCL, Opt. Express 21 (2013) 1008–1019.
[79] P. Patimisco, S. Borri, I. Galli, D. Mazzotti, G. Giusfredi, N. Akikusa, M. Yamanishi, G. Scamarcio, P. De Natale, V. Spagnolo, High finesse optical cavity coupled with a quartz-enhanced photoacoustic spectroscopic sensor, Analyst 140 (2015) 736–743.
[80] S. Borri, P. Patimisco, I. Galli, D. Mazzotti, G. Giusfredi, N. Akikusa, M. Yamanishi, G. Scamarcio, P. De Natale, V. Spagnolo, Intracavity quartz-enhanced photoacoustic sensor, Appl. Phys. Lett. 104 (2014) 091114.
[81] P. Patimisco, A. Sampaolo, F.K. Tittel, V. Spagnolo, Mode matching of a laser-beam to a compact high finesse bow-tie optical cavity for quartz enhanced photoacoustic gas sensing, Sens. Actuators A 267 (2017) 70–75.
[82] Q. Wang, Z. Wang, W. Ren, P. Patimisco, A. Sampaolo, V. Spagnolo, Fiber-ring laser intracavity QEPAS gas sensor using a 7.2 kHz quartz tuning fork, Sensors Actuators B Chem. 268 (2018) 512–518.
[83] A.A. Kosterev, T.S. Mosely, F.K. Tittel, Impact of humidity on quartz-enhanced photoacoustic spectroscopy based detection of HCN, Appl. Phys. B Lasers Opt. 85 (2006) 295–300.
[84] F.K. Tittel, A. Sampaolo, P. Patimisco, L. Dong, A. Geras, T. Starecki, V. Spagnolo, Analysis of overtone flexural modes operation in quartz-enhanced photoacoustic spectroscopy, Opt. Express 24 (2016) A682–A692.
[85] A. Sampaolo, P. Patimisco, L. Dong, A. Geras, G. Scamarcio, T. Starecki, F.K. Tittel, V. Spagnolo, Quartz-enhanced photoacoustic spectroscopy exploiting tuning fork overtone modes, Appl. Phys. Lett. 107 (2015) 231102.
[86] F.R. Blom, S. Bouwstra, M. Elwenspoek, J.H.J. Fluitman, Dependence of the quality factor of micromachined silicon beam resonators on pressure and geometry, J. Vac. Sci. Technol. B 10 (1992) 19–26.

[87] K. Kokubun, M. Hirata, M. Ono, H. Murakami, Y. Toda, Frequency dependence of a quartz oscillator on gas pressure, J. Vac. Sci. Technol. A 3 (1985) 2184–2187.
[88] W.E. Newell, Miniaturization of tuning forks, Science 161 (1968) 1320–1326.
[89] M. Christen, Air and gas damping of quartz tuning forks, Sensors Actuators 4 (1983) 555–564.
[90] H. Hosaka, K. Itao, S. Kuroda, Damping characteristics of beam-shaped micro-oscillators, Sensors Actuators B Chem. 49 (1995) 87–95.
[91] K. Kokubun, H. Murakami, Y. Toda, M. Ono, A bending and stretching mode crystal oscillator as a friction vacuum gauge, Vacuum 34 (1984) 731–735.
[92] Y. Jimbo, K. Itao, Energy loss of a cantilever vibrator, J. Horolog. Inst. Jpn. 47 (1968) 1–15.
[93] D.M. Photiadisa, J.A. Judge, Attachment losses of high Q oscillators, Appl. Phys. Lett. 85 (2005) 482–484.
[94] Z. Hao, A. Erbil, F. Ayazi, An analytical model for support loss in micromachined beam resonators with in-plane flexural vibrations, Sensors Actuators B Chem. 109 (2003) 156–164.
[95] J.A. Judge, D.M. Photiadis, J.F. Vignola, B.H. Houston, J. Jarzynski, Attachment loss of micromechanical and nanomechanical resonators in the limits of thick and thin support structures, J. Appl. Phys. 101 (2007) 013521: 1-013521:11.
[96] C. Zener, Internal friction in solids II. General theory of thermoelastic internal friction, Phys. Rev. 53 (1938) 90–99.
[97] P. Patimisco, A. Sampaolo, M. Giglio, V. Mackoviak, H. Rossmadl, B. Gross, A. Cable, F.K. Tittel, V. Spagnolo, Octupole electrode pattern for tuning forks vibrating at the first overtone mode in quartz-enhanced photoacoustic spectroscopy, Opt. Lett. 43 (2018) 1854–1857.
[98] P. Patimisco, A. Sampaolo, L. Dong, F.K. Tittel, V. Spagnolo, Recent advances in quartz enhanced photoacoustic sensing, Appl. Phys. Rev. 5 (2018) 011106.
[99] A. Sampaolo, P. Patimisco, M. Giglio, M.S. Vitiello, H.E. Beere, D.A. Ritchie, G. Scamarcio, F.K. Tittel, V. Spagnolo, Improved tuning fork for terahertz quartz-enhanced photoacoustic spectroscopy, Sensors 16 (2016) 439. 1-439:8.
[100] S. Borri, P. Patimisco, A. Sampaolo, H.E. Beere, D.A. Ritchie, M.S. Vitiello, G. Scamarcio, V. Spagnolo, Terahertz quartz enhanced photo-acoustic sensor, Appl. Phys. Lett. 103 (2013) 021105.
[101] A. Castellanos-Gomez, N. Agraït, G. Rubio-Bollinger, Dynamics of quartz tuning fork force sensors used in scanning probe microscopy, Nanotechnology 20 (2009) 215502: 1-215502:8.
[102] J. Rychen, T. Ihn, P. Studerus, A. Herrmann, K. Ensslin, A low-temperature dynamic mode scanning force microscope operating in high magnetic fields, Rev. Sci. Instrum. 70 (1999) 2765–2768.
[103] H. Wu, A. Sampaolo, L. Dong, P. Patimisco, X. Liu, H. Zheng, X. Yin, W. Ma, L. Zhang, W. Yin, V. Spagnolo, S. Jia, F.K. Tittel, Quartz enhanced photoacoustic H_2S gas sensor based on a fiber-amplifier source and a custom tuning fork with large prong spacing, Appl. Phys. Lett. 107 (2015) 111104.
[104] P. Patimisco, A. Sampaolo, H. Zheng, L. Dong, F.K. Tittel, V. Spagnolo, Quartz–enhanced photoacoustic spectrophones exploiting custom tuning forks: a review, Adv. Phys. X 2 (2016) 169–187.
[105] H. Zheng, L. Dong, A. Sampaolo, H. Wu, P. Patimisco, X. Yin, W. Ma, L. Zhang, W. Yin, V. Spagnolo, S. Jia, F.K. Tittel, Single-tube on-beam quartz-enhanced photoacoustic spectroscopy, Opt. Lett. 41 (2016) 978–981.

[106] H. Zheng, L. Dong, A. Sampaolo, P. Patimisco, W. Ma, L. Zhang, W. Yin, L. Xiao, V. Spagnolo, S. Jia, F.K. Tittel, Overtone resonance enhanced single-tube on-beam quartz enhanced photoacoustic spectrophone, Appl. Phys. Lett. 109 (2016) 111103.
[107] H. Zheng, L. Dong, P. Patimisco, H. Wu, A. Sampaolo, X. Yin, S. Li, W. Ma, L. Zhang, W. Yin, L. Xiao, V. Spagnolo, S. Jia, F.K. Tittel, Double antinode excited quartz-enhanced photoacoustic spectrophone, Appl. Phys. Lett. 110 (2017) 021110.
[108] H. Wu, X. Yin, L. Dong, K. Pei, A. Sampaolo, P. Patimisco, H. Zheng, W. Ma, L. Zhang, W. Yin, L. Xiao, V. Spagnolo, S. Jia, F.K. Tittel, Simultaneous dual-gas QEPAS detection based on a fundamental and overtone combined vibration of quartz tuning fork, Appl. Phys. Lett. 110 (2017) 121104.
[109] A. Pohlkotter, M. Koehring, U. Willer, W. Schade, Detection of molecular oxygen at low concentrations used quartz enhanced photoacoustic spectroscopy, Sensors 10 (2010) 8466–8477.
[110] Y. Ma, Y. He, Y. Tong, X. Yu, F.K. Tittel, Ppb-level detection of ammonia based on QEPAS using a power amplified laser and a low resonance frequency quartz tuning fork, Opt. Express 25 (2017) 29356–29364.
[111] L. Dong, A.A. Kosterev, D. Thomazy, F.K. Tittel, Compact portable QEPAS multi-gas sensor, Proc. SPIE 7945 (2011) 79450R. 1–79450R:7.
[112] A. Sampaolo, S. Csutak, P. Patimisco, M. Giglio, G. Menduni, V. Passaro, F.K. Tittel, M. Deffenbaugh, V. Spagnolo, Interband cascade laser based quartz-enhanced photoacoustic sensor for multiple hydrocarbons detection, Proc. SPIE 10540 (2018) 105400C.
[113] A. Sampaolo, S. Csutak, P. Patimisco, M. Giglio, G. Menduni, V. Passaro, F.K. Tittel, M. Deffenbaugh, V. Spagnolo, Methane, ethane and propane detection using a compact quartz enhanced photoacoustic sensor and a single interband cascade laser, Opt. Express 282 (2019) 952–960.
[114] M. Horstjann, Y.A. Bakhirkin, A.A. Kosterev, R.F. Curl, F.K. Tittel, C.M. Wong, C.J. Hill, R.Q. Yang, Formaldehyde sensor using interband cascade laser based quartz-enhanced photoacoustic spectroscopy, Appl. Phys. B Lasers Opt. 79 (2004) 799–803.
[115] F.K. Tittel, G. Wysocki, A.A. Kosterev, Y.A. Bakhirkin, Semiconductor laser based trace gas sensor technology: recent advances and applications, in: Mid-Infrared Coherent Sources and Applications, Springer, Houten, The Netherlands, 2007, pp. 467–493.
[116] R. Lewicki, J. Waclawek, M. Jahjah, Y. Ma, E. Chrysostom, B. Lendl, F.K. Tittel, A sensitive CW DFB quantum cascade laser based QEPAS sensor for detection of SO_2. CLEO: Appl. Technol. (2012), https://doi.org/10.1364/CLEO_AT.2012.ATh5A.3.
[117] W. Ren, W. Jiang, N.P. Sanchez, P. Patimisco, V. Spagnolo, C. Zah, F. Xie, L.C. Hughes, R.J. Griffin, F.K. Tittel, Hydrogen peroxide detection with quartz-enhanced photoacoustic spectroscopy using a distributed-feedback quantum cascade laser, Appl. Phys. Lett. 104 (2014) 041117.
[118] M. Jahjah, W. Jiang, N.P. Sanchez, W. Ren, P. Patimisco, V. Spagnolo, S.C. Herndon, R.J. Griffin, F.K. Tittel, Atmospheric CH_4 and N_2O measurements near Greater Houston area landfills using a QCL based QEPAS sensor system during DISCOVER-AQ 2013, Opt. Lett. 39 (2014) 957–960.
[119] P. Patimisco, A. Sampaolo, M. Giglio, F. Sgobba, H. Rossmadl, V. Mackowiak, B. Gross, A. Cable, F.K. Tittel, V. Spagnolo, Compact and low-noise quartz-enhanced photoacoustic sensor for sub-ppm ethylene detection in atmosphere, Proc. SPIE 10540 (2018) 105401Q.
[120] V. Spagnolo, P. Patimisco, R. Pennetta, A. Sampaolo, G. Scamarcio, M.S. Vitiello, F.K. Tittel, THz Quartz-enhanced photoacoustic sensor for H_2S trace gas detection, Opt. Express 23 (2015) 7574–7582.

[121] A.A. Kosterev, Y.A. Bakhirkin, F.K. Tittel, Ultrasensitive gas detection by quartz-enhanced photoacoustic spectroscopy in the fundamental molecular absorption bands region, Appl. Phys. B Lasers Opt. 80 (2005) 133–138.
[122] A.A. Kosterev, Y.A. Bakhirkin, F.K. Tittel, S. Blaser, Y. Bonetti, L. Hvozdara, Photoacoustic phase shift as a chemically selective spectroscopic parameter, Appl. Phys. B Lasers Opt. 78 (2004) 673–676.
[123] P. Werle, R. Miicke, F. Slemr, The limits of signal averaging in atmospheric trace-gas monitoring by tunable diode-laser absorption spectroscopy (TDLAS), Appl. Phys. B Lasers Opt. 57 (1993) 131–139.
[124] M. Giglio, P. Patimisco, A. Sampaolo, G. Scamarcio, F.K. Tittel, V. Spagnolo, Allan deviation plot as a tool for quartz enhanced photoacoustic sensors noise analysis, IEEE Trans. Ultrason. Ferroelectr. Freq. Control 63 (2016) 555–560.
[125] A. Kachanov, S. Koulikov, F.K. Tittel, Cavity enhanced optical feedback assisted photoacoustic spectroscopy with a 10.4 microns external-cavity quantum cascade laser, Appl. Phys. B Lasers Opt. 110 (2013) 47–56.
[126] M. Jahjah, W. Ren, P. Stefanski, R. Lewicki, J. Zhang, W. Jiang, J. Tarka, F.K. Tittel, A compact QCL based methane and nitrous oxide sensor for environmental and medical applications, Analyst 139 (2014) 2065–2069.
[127] S.T. Moe, K. Schjølberg-Henriksen, D.T. Wang, E. Lund, J. Nysæther, L. Furuberg, M. Visser, T. Fallet, R.W. Bernstein, Capacitive differential pressure sensor for harsh environments, Sensors Actuators B Chem. 83 (2000) 30–33.
[128] L.G. Harus, M. Cai, K. Kawashima, K. Toshiharu, Determination of temperature recovery time in differential-pressure-based air leak detector, Meas. Sci. Technol. 17 (2006) 411–418.
[129] P.E. Mix, Leak testing methods, in: Introduction to Nondestructive Testing: A Training Guide, John Wiley & Sons, Inc., 2004.
[130] S. Millar, M. Desmulliez, MEMS ultra low leak detection methods: a review, Sens. Rev. 29 (2009) 339–344.
[131] S. Kai-lei, S. Xin-li, Summary of the theory and method of vacuum helium-mass-spectroscopy leak detection, Vacuum Electronics 6 (2007) 62–65.
[132] A. Calcatelli, M. Bergoglio, D. Mari, Leak detection, calibrations and reference flows: practical example, Vacuum 81 (2007) 1538–1544.
[133] A. Sampaolo, P. Patimisco, M. Giglio, L. Chieco, G. Scamarcio, F.K. Tittel, V. Spagnolo, Highly sensitive gas leak detector based on a quartz-enhanced photoacoustic SF6 sensor, Opt. Express 24 15872-15881.
[134] G. Cheng, Y. Cao, K. Liu, G. Zhu, G. Wang, X. Gao, Photoacoustic measurement of ethane with near-infrared DFB diode laser, J. Spectrosc. (2018). (2018) 9765806.
[135] C.R. Webster, Measuring methane and its isotopes $^{12}CH_4$, $^{13}CH_4$ and CH_3D on the surface of Mars with in situ laser spectroscopy, Appl. Opt. 44 (2005) 1226–1235.
[136] https://www.pnnl.gov/.
[137] A. Berna, Metal oxide sensors for electronic noses and their application to food analysis, Sensors 10 (2010) 3882–3910.
[138] A. Sklorz, S. Janßen, W. Lang, Detection limit improvement for NDIR ethylene gas detectors using passive approaches, Sensors Actuators B Chem. 176 (2012) 246–254.
[139] S. Janssen, T. Tessmann, W. Lang, High sensitive and selective ethylene measurement by using a large capacity-on-chip preconcentrator device, Sensors Actuators B Chem. 197 (2014) 405–413.
[140] http://www.hitran.org/.